The Astrophysical Journal, 990:51 (26pp), 2025 September 1 https://doi.org/10.3847/1538-4357/adea94

Spatially Resolved Kinematics of SLACS Lens Galaxies. I. Data and Kinematic Classification

Shawn Knabel[1], Tommaso Treu[1], Michele Cappellari[2], Anowar J. Shajib[3,4,5,8], Chih-Fan Chen[1], Simon Birrer[6], and Vardha N. Bennert[7]
[1] Department of Physics and Astronomy, University of California, Los Angeles, CA 90095, USA; shawnknabel@astro.ucla.edu
[2] Sub-Department of Astrophysics, Department of Physics, University of Oxford, Denys Wilkinson Building, Keble Road, Oxford OX1 3RH, UK
[3] Department of Astronomy & Astrophysics, University of Chicago, Chicago, IL 60637, USA
[4] Kavli Institute for Cosmological Physics, University of Chicago, Chicago, IL 60637, USA
[5] Center for Astronomy, Space Science and Astrophysics, Independent University, Bangladesh, Dhaka 1229, Bangladesh
[6] Department of Physics and Astronomy, Stony Brook University, Stony Brook, NY 11794, USA
[7] Physics Department, California Polytechnic State University, San Luis Obispo, CA 93407, USA
Received 2024 March 1; revised 2025 May 28; accepted 2025 June 27; published 2025 August 25

Abstract

We obtain spatially resolved kinematics with the Keck Cosmic Web Imager (KCWI) integral-field spectrograph for a sample of 14 massive ($11 < \log_{10} M_*/M_\odot < 12$) lensing early-type galaxies at $z \sim 0.15$–0.35 from the Sloan Lens ACS (SLACS) Survey. We integrate kinematic maps within the galaxy effective radius and examine the rotational and dispersion velocities, showing that $11/14$ can be classified as slow rotators. The data set is unprecedented for galaxy-scale strong lenses in terms of signal-to-noise ratio (S/N), sampling, and calibration, vastly superseding previous studies. We find the primary contributions to systematic uncertainties to be the stellar template library and wavelength range of the spectral fit. Systematics are at the 1%–1.4% level, and positive covariance is <1% between sample galaxies and between spatial bins. This enables cosmographic inference with lensing time delays with a <2% uncertainty on H_0. We examine the effects of integration of the data cubes within circular apertures of different sizes and compare with Sloan Digital Sky Survey (SDSS) single-aperture velocity dispersions. We conclude that the velocity dispersions extracted from SDSS spectra for these 14 SLACS galaxies, which have low S/N ($\sim$9 Å^{-1}) relative to the SLACS candidate parent sample, are subject to systematic errors (and covariance) due to stellar template library selection at the level of 3% (2%), which need to be added to the random errors. Comparison between our KCWI stellar velocity dispersions, our own analysis of SDSS spectra, and previously published measurements based on SDSS spectra shows mean differences within a few percent. However, these differences are not significant given the uncertainties of the SDSS-based stellar velocity dispersions. We find that the correlations between scaling relations using quantities inferred from dynamical, lensing, and stellar population models agree with previous SLACS analysis with no statistically significant change. A follow-up paper will present Jeans modeling in the context of broader studies of galaxy evolution and cosmology.

Unified Astronomy Thesaurus concepts: Galaxies (573); Early-type galaxies (429); Galaxy kinematics (602); Galaxy dynamics (591); Observational cosmology (1146); Hubble constant (758)

1. Introduction

Morphological classification of galaxies began the dialog between evolutionary theories and observations, which led to our current understanding of the variety of galaxy properties in our Universe (E. P. Hubble 1926; A. Sandage 1975, 2005; J. Kormendy & R. Bender 2009, 2012; A. W. Graham 2013). In the picture of hierarchical galaxy assembly described in a Lambda cold dark matter (ΛCDM) cosmology, early-type galaxies (ETGs) are thought to be the end products of these evolutionary paths (A. Burkert & T. Naab 2004; G. De Lucia et al. 2006). Consequentially, ETGs are important observational tests of our knowledge of the Universe.

1.1. Kinematics

Observations of ETGs have led to powerful empirical scaling relationships like the fundamental plane (FP) of ETGs that help us to understand the formation and evolution of these galaxies (S. M. Faber & R. E. Jackson 1976; J. Kormendy 1977; S. Djorgovski & M. Davis 1987; A. Dressler et al. 1987; M. Cappellari et al. 2006; A. Renzini 2006; A. S. Bolton et al. 2007). One of the key insights of the FP is a correlation between the line-of-sight stellar velocity dispersion and several fundamental galaxy properties. Measurements of elliptical galaxy kinematics with spectroscopy have therefore been very scientifically productive, yielding a wealth of insights into their dynamics, formation, and evolution (see, e.g., M. Cappellari 2016 for a review). Integrated line-of-sight velocity dispersions of ETGs from single-aperture spectroscopy have contributed significantly to the characterization of the masses of distant galaxies through dynamical inferences and joint analysis with other mass measurements, e.g., gravitational lens models (M. W. Auger et al. 2009, 2010a, henceforth SLACS-IX and SLACS-X) and stellar population studies.

[8] NFHP Einstein Fellow.

Galaxy kinematics studies gained an additional dimension with the advent and now ubiquity of integral-field spectrographs (IFSs) on most major observatories (R. Bacon et al. 1995, 2001, 2010; P. Morrissey et al. 2012; e.g., TIGER, SAURON, MUSE, and the Keck Cosmic Web Imager (KCWI)). This technology allows spatially resolved velocity measurements because each spatial pixel (or spaxel) is dispersed into an individual spectrum.

This gives a 2D projection of the stellar velocity distributions within the galaxy. Dynamical arguments and other physical constraints allow one to deproject and constrain the intrinsic 3D stellar orbits, which trace the gravitational potential of the galaxy. The 3D nature of the stellar orbits encoded in the observable 2D kinematics are described by anisotropy parameters, which quantify how the stellar velocity ellipsoid (in velocity space) at a given spatial coordinate deviates from an isotropic case (i.e., there is a preferred direction of stellar velocities).

Studies of elliptical galaxy isophotes (J. Kormendy & R. Bender 1996; S. M. Faber et al. 1997; J. Kormendy & R. Bender 2012; J. Kormendy & K. C. Freeman 2016) and kinematics revealed a dichotomy that prescribes two distinct classes of ETGs. The SAURON survey (R. Bacon et al. 2001; P. T. de Zeeuw et al. 2002) used the SAURON IFS on the William Herschel Telescope and Hubble Space Telescope (HST) images to study the kinematics of galaxies in the local Universe (E. Emsellem et al. 2004, 2007; M. Cappellari et al. 2006, 2007). This and other studies with IFSs (M. Cappellari et al. 2011; D. Krajnovic 2011; J. J. Bryant et al. 2015; K. Bundy et al. 2015; ATLAS^{3D}, SAMI, and the Sloan Digital Sky Survey (SDSS) MaNGA) have opened new kinematic-based galaxy-classification schemes and offered insights to the formation mechanisms of ETGs (see M. Cappellari 2016 for a full review). Many galaxies that appear to be elliptical are in fact better described as rotationally supported, flattened disks with significant bulge components and low star formation. Their elliptical appearance stems from projection effects. The kinematic properties of these rotating ellipticals challenge an evolutionary scenario where growth and star formation quenching are dominated by major mergers. Instead, a large contributor to their growth must come from minor "wet" (i.e., gas-rich) mergers and the accretion of gas from the surrounding galactic medium, with star formation being quenched by internal mechanisms (E. Cheung et al. 2012; J. J. Fang et al. 2013). In fact, the parameter space of features that describe nearby younger disk galaxies and their disky elliptical cousins overlaps considerably (J. Falcón-Barroso et al. 2015; M. Querejeta et al. 2015). The disks masquerading as ETGs appear to be once star-forming galaxies that were lucky enough to lead a relatively merger-less life and so retain their disky identity. The cases that resemble the more classic elliptical picture are likely the result of mergers (e.g., R. Bezanson et al. 2009; T. Naab et al. 2009; P. F. Hopkins et al. 2010). These two classes have been termed "fast (or regular) rotators" and "slow (or nonregular) rotators," as they can be distinctly classified with significantly different kinematic attributes (M. Cappellari et al. 2007; E. Emsellem et al. 2007).

1.2. Dynamics and Strong Gravitational Lensing

Dynamical mass models of ETGs with IFS spatially resolved kinematics (e.g., SAURON, ATLAS^{3D}, etc.) have been created using solutions to the two- and three-integral Jeans equations of stellar hydrodynamics in spherical and axisymmetric alignments (E. Emsellem et al. 1994; M. Cappellari 2008), and more generally with M. Schwarzschild (1979) models of orbital superposition generalized to fit kinematic data (D. O. Richstone & S. Tremaine 1988; H.-W. Rix et al. 1997; R. P. van der Marel et al. 1998). These lead to robust measurements of the total mass content (baryonic and dark) and the mass density profiles of these galaxies, which have been shown to be in excellent agreement with mass measurements obtained with strong gravitational lensing. Studies of lensing ETGs have shown them to be indistinct from other ETGs in the observed mass range (SLACS-IX), which tend to be relatively large compared to the overall population of ETGs due to the strong dependence of lensing optical depth on velocity dispersion (Y. Shu et al. 2015; S. Knabel et al. 2020). In the mid 2000s, the Sloan Lens ACS (SLACS) Survey produced a wealth of papers (e.g., A. S. Bolton et al. 2006; L. V. E. Koopmans et al. 2006; T. Treu et al. 2006; etc.) utilizing strong gravitational lensing and other observables to study the properties of a definitive sample of 85 large early-type gravitational lenses (plus another 100 or so in additional follow-up surveys). These galaxies were identified spectroscopically as strong-lensing candidates in the SDSS and confirmed with HST/ACS. The resulting sample combined strong lens models and single-aperture velocity dispersions to jointly constrain the mass profiles and fundamental scaling relations (A. S. Bolton et al. 2008b; SLACS-IX, SLACS-X). SLACS is perhaps the most well-studied set of gravitational lenses, having been followed-up by several additional independent observations and analyses. For example, O. Czoske et al. (2008, 2012) used Very Large Telescope (VLT) VIMOS integral-field unit (IFU) observations to determine spatially resolved stellar kinematics of several SLACS lenses, providing a first comparison to IFS kinematic surveys of more nearby galaxies like SAURON (E. Emsellem et al. 2004) and ATLAS^{3D} (M. Cappellari et al. 2011).

1.3. Time-delay Cosmography and Overcoming Degeneracies

A large effort has been undertaken in the past two decades to independently measure H_0 through time-delay cosmography of lensed quasars (S. Refsdal 1964); for up-to-date reviews, see S. Birrer et al. (2024) and T. Treu et al. (2022); for a historical perspective, see T. Treu & P. J. Marshall (2016). The Time-Delay Cosmography (TDCOSMO) collaboration has analyzed seven time-delay lenses to measure the Hubble constant within a 2% error ($H_0 = 74.2 \pm 1.6\,\mathrm{km\,s^{-1}\,Mpc^{-1}}$) assuming simple parametric mass profiles for the lensing galaxies (M. Millon et al. 2020b). TDCOSMO encompasses the Cosmological Monitoring of Gravitational Lenses (COSMOGRAIL; F. Courbin et al. 2005; M. Millon et al. 2020a), the H_0 Lenses in COSMOGRAIL's Wellspring (V. Bonvin et al. 2017; S. H. Suyu et al. 2017; S. Birrer et al. 2019; C. E. Rusu et al. 2020; K. C. Wong et al. 2020), the Strong-lensing High Angular Resolution Programme (Y.-M. Chen et al. 2019), and the Strong-lensing Insights into the Dark Energy Survey (T. Treu et al. 2018; A. J. Shajib et al. 2021; T. Schmidt et al. 2023) collaborations.

An important and delicate caveat in the application of lens modeling methods is called the "mass-sheet degeneracy" (MSD), which can be succinctly described as the nonuniqueness of mass profile solutions that can result in the observed lensed image features (E. E. Falco et al. 1985; P. Schneider & D. Sluse 2013, 2014). The TDCOSMO collaboration has

tested several potential sources of uncertainty and concluded that the MSD is the most significant source of uncertainty in the measurement of H_0 with time-delay cosmography of lensed quasars (S. Birrer et al. 2020; D. Gilman et al. 2020; M. Millon et al. 2020b; A. J. Shajib et al. 2022; L. Van de Vyvere et al. 2022a, 2022b). A nonlensing tracer of gravitational potential (e.g., kinematics) is required to break the degeneracy (T. Treu & L. V. E. Koopmans 2002; SLACS-X; A. J. Shajib et al. 2018; A. Yıldırım et al. 2020, 2023). Using single-aperture velocity dispersions, while allowing for more flexible mass models, S. Birrer et al. (2020; henceforth TDCOSMO-IV) measured H_0 to within 8% precision ($H_0 = 74.5^{+5.6}_{-6.1}$ km s^{-1} Mpc^{-1}) using just seven time-delay lenses.

Line-of-sight velocity dispersions from single-aperture spectroscopy can constrain galaxy dynamics, but there exists another degeneracy, the mass–anisotropy degeneracy (MAD; J. Binney & G. A. Mamon 1982), which cannot be broken without spatially resolved kinematics (M. Cappellari 2008; M. Barnabè et al. 2009, 2011; T. E. Collett et al. 2018; A. J. Shajib et al. 2018, 2023; S. Birrer & T. Treu 2021). MAD arises because we cannot observe all components of the stellar velocities, but only their projection along the line of sight. The anisotropy parameter $\beta_{\rm ani}$ that encodes this information is the crucial unknown component. Studies of nearby ETGs like the SAURON survey (M. Cappellari et al. 2007; E. Emsellem et al. 2007) show that this anisotropy is not a universal parameter, nor is it radially uniform within a single galaxy. Anisotropy profiles can be illuminated with the study of spatially resolved kinematics. Breaking either the MSD or MAD on its own is a daunting task, but the union of lensing and dynamics can put joint constraints on both. This is the strategy outlined by A. J. Shajib et al. (2018) and S. Birrer & T. Treu (2021), and demonstrated by A. J. Shajib et al. (2023; henceforth TDCOSMO-XII) using KCWI resolved kinematics of the quasar time-delay lens RXJ1131-1231 to constrain H_0 within a 9% error for the single lens (comparable to the sample of seven lenses in TDCOSMO-IV). Additional constraints can be placed on these cosmography measurements by auxiliary observations of non-time-delay (i.e., the lensed source is not variable in time) lensing galaxies as in TDCOSMO-IV. Through Bayesian hierarchical inference, constraints from the population level increase the precision of time-delay lens analysis. TDCOSMO-IV used single-aperture SDSS (Y. Shu et al. 2015, henceforth SLACS-XII) and VLT/VIMOS IFU (O. Czoske et al. 2008, 2012) kinematics from 33 SLACS lenses to increase the precision of their sample from 8% to 5%.

However, the kinematic data need to have sufficient signal-to-noise ratio (S/N) and spectral resolution to enable measurements of the Hubble constant with the precision and accuracy required to help settle the 8% difference between the early and late Universe probes (e.g., E. Abdalla et al. 2022, and references therein). The relative error on the Hubble constant is to first order equal to double the relative error on stellar velocity dispersion ($\delta H_0/H_0 \approx 2\delta\sigma/\sigma$; e.g., Q. Chen et al. 2021). Whereas random errors can be constrained with larger samples, it is crucial to mitigate the systematic bias and covariance within and between data sets, ideally to the subpercent level. Reaching this goal is possible with data of sufficient resolution and S/N, if the data and stellar templates are clean of defects and careful methods are applied for extracting the kinematics (S. Knabel et al. 2025).

Unfortunately, the VLT/VIMOS IFU data had insufficient spatial sampling ($0\farcs67$ spaxel^{-1}) and spectral resolution ($R \sim 2500$) to reach the precision and accuracy required to overcome the MAD and measure H_0 to our desired levels. Furthermore, VIMOS, as a fiber-based first-generation IFS on VLT, did not have the stability and accuracy of sky subtraction and wavelength and resolution calibration of modern day IFSs such as KCWI and MUSE. TDCOSMO-IV found VIMOS data to require a significant error boost to account for systematic uncertainties. They did not utilize the absolute measurements of the velocity dispersion and instead used only the relative shape to constrain the MAD. Likewise, the SDSS data of the SLACS lenses had limited S/N (S. Knabel et al. 2025), and stellar velocity dispersions had been measured for galaxy formation and evolution purposes and not with precision cosmography in mind. Systematic errors were thought to be at the 5% level (A. S. Bolton et al. 2008a; Y. Shu et al. 2015).

We present spatially resolved kinematics of a selection of 14 strong-lensing ETGs selected from the SLACS catalog. The SLACS Survey is an ideal parent sample from which to select our sample for the wealth of auxiliary data and measurements that exist and their observability in terms of size and brightness. The resolution ($R \sim 3600$), spatial sampling (spaxel size of $0\farcs1457 \times 0\farcs1457$), and subarcsecond seeing (average $0\farcs9$ across the observing dates) afforded by Keck and KCWI offer a more detailed description of the 2D velocity distribution than any previous kinematics study of these galaxies. In order to minimize systematic errors and take full advantage of the high quality of our spectroscopic data, we adopt the recently developed methods and clean stellar libraries described by S. Knabel et al. (2025; henceforth TDCOSMO-XIX). Lensing models have been conducted in a uniform manner for all objects in our sample by C. Y. Tan et al. (2024). New dynamical models for each galaxy are being computed via Jeans anisotropic modeling (JAM, M. Cappellari 2008, 2020) and will be presented in a follow-up paper (Paper II).

Observations were taken with KCWI and are presented in Section 2. Kinematic analysis methods are described in Section 3, including systematic and random error estimates, estimated on the basis of the methods recently developed in TDCOSMO-XIX. Kinematic maps and initial results, including kinematic classification and aperture-integrated kinematics, are introduced in Section 4. Correlations between kinematics and other observables are discussed in Section 5.1. Additional points of discussion are considered in Section 5, and finally we summarize our results in Section 6. Where necessary, we assume a standard ΛCDM cosmology with $\Omega_m = 0.3$ and $H_0 = 70$ km s^{-1} Mpc^{-1}. We note of course that stellar velocity dispersions are independent of cosmology.

2. Observations

We select 14 objects from the SLACS Survey that have been uniformly modeled by C. Y. Tan et al. (2024). The sample is representative of the parent sample, being selected mostly based on observability, decl., and R.A., according to when telescope time was scheduled. Spectra were observed with KCWI (P. Morrissey et al. 2012, 2018) on Keck II during both 2021 semesters and the first semester of 2022 (nights of 2021 May 6 and 15, June 7, August 12, and November 26; and 2022 April 7). See Table 1 for the average seeing estimates obtained at the telescope on the dates of observation.

Table 1
Average Seeing Estimates from the Telescope Focus on the Dates of Observation with KCWI

Observing Date	Average Seeing (arcsec)
2021 May 7	1.08
2021 May 16	1.2
2021 Jun 8	0.5
2021 Aug 13	1.2
2021 Nov 27	0.8
2022 Apr 8	0.9

At redshifts around $z \sim 0.15$–0.35, an S/N of ~10 can be achieved with 2–3 hr of exposure. As in TDCOSMO-XII we take a series of 30 minute exposures with the low-resolution blue grating centered at 4600 Å with the small slicer and 1×1 binning. The spectral resolution of $R \sim 3600$ corresponds to an instrumental dispersion $\sigma_{\rm inst} = 35\,{\rm km\,s^{-1}}$. The reciprocal dispersion is 0.5 Å pixel^{-1}. We dither by around 8″ along the long axis of the $8\farcs4 \times 20\farcs4$ field of view to obtain background sky simultaneously with the on-source exposure for sky subtraction. Standard stars are observed periodically through the night for calibration.

The resulting 4–5 exposures for each object are reduced with the KCWI official Python-based data reduction pipeline (developed by Luca Rizzi, Don Neill, and Max Brodheim).[9] The pipeline translates the 2D information from the detector into a 3D data cube, performing geometry correction, differential atmospheric refraction correction, wavelength calibration, and standard-star calibration. The calibration with the standard star corrects for instrumental response and scales the data to flux units (P. Morrissey et al. 2018). We use the final output files with the suffix "icubes" and create mosaics from the frames by drizzling (A. S. Fruchter & R. N. Hook 2002). Drizzling is performed using a modification of the routine utilized in the official Keck OSIRIS IFU pipeline, using recommended settings (R. Avila et al. 2015). Throughout the drizzling process, the rectangular ($0\farcs1457 \times 0\farcs3395$) geometry of KCWI pixels is maintained. We transform to square pixels of dimensions $0\farcs1457 \times 0\farcs1457$ after drizzling by resampling to conserve flux.

In order to measure the point-spread function (PSF), we sum the data cube across wavelength bins to create a 2D image, which we show in Figure 1. HST imaging is available for each of these objects (ACS Wide Field Channel (WFC) F814W and F435W, and WFPC2 F606W; HST-SNAP 10174; HST-GO 10494, 10886, 10798, and 11202; PIs: Koopmans and Bolton). We convolve the high-resolution HST image with a Gaussian PSF kernel and fit to the KCWI summed data cube for optimal values of the PSF width σ, with two additional parameters to correct for offset of the two images. Surface brightness profiles from HST also allow us to examine the kinematic structure in relation to the morphology, especially the alignment (or misalignment) of the kinematic and photometric major axes. The kinematic maps and photometry are aligned with the brightest pixels in the central foreground deflecting galaxy. We take B-spline models and PSF models from A. S. Bolton et al. (2008a) for these HST images. We use multi-Gaussian expansion (MGE; E. Emsellem et al. 1994; M. Cappellari 2002) to translate the B-spline models and PSF models (for both KCWI and HST data) to a parameterization that is ideal for future dynamical fitting.

[9] https://kcwi-drp.readthedocs.io/

3. Kinematic Measurements

The spatially resolved kinematics analysis is done with Penalized Pixel-Fitting (pPXF) method[10] (M. Cappellari & E. Emsellem 2004; M. Cappellari 2017, 2023), which extracts stellar kinematics by fitting the observed spectrum with a linear combination of template stellar spectra convolved with (broadened by) a line-of-sight velocity distribution (LOSVD) constructed with a Gauss–Hermite parameterization. Observed and template spectra are all logarithmically rebinned before fitting. Additive Legendre polynomials give greater fitting power by adjusting the strength of individual absorption lines (see M. Cappellari 2017 for a full description), and multiplicative polynomials account for inaccuracies in the relative spectral flux calibration (see TDCOSMO-XIX for further discussion).

Traditionally, the singly-ionized calcium (Ca II) H and K stellar absorption lines (3934 and 3969 Å, hereafter CaHK) have been used to measure stellar kinematics (see, e.g., A. Dressler 1979). CaHK are very strong and intrinsically broad features, which makes them ideal for detections with low brightness and low S/N. Discussion of the consistency of CaHK kinematics (e.g., J. Kormendy & G. Illingworth 1982; E. J. Murphy et al. 2011) have become insignificant since PPXF standardized the practice of using linear combinations of multiple templates from a flexible stellar library. Alternative features throughout all wavelength ranges have also been used. The redshifted CaHK lines for all objects are present well within the observed wavelength range (3500–5600 Å). Na D and Mg I lines will be redshifted beyond 5600 Å for all objects ($z \sim 0.15$–0.35). *G*-band absorption due to CH and neutral Fe (rest-frame 4304 Å) is observable for all but one target (SDSS J0330−0020 at $z = 0.351$). Our extracted kinematics are unbiased when excluding the *G*-band, and we take full advantage of all the available line features for each individual object in the sample. Our baseline extraction wavelength range is 3600–4500 Å. The blue cutoff is set by the quality requirements on the template stellar spectra, which have low S/N and imperfect calibration at shorter wavelength (TDCOSMO-XIX). The red cutoff is set by the need to have a uniform wavelength range and capture the *G*-band. We examine the effects of the selection of wavelength range, as well as other systematics, in Section 3.1.

In principle, kinematics can be measured for each spaxel in the data cube. Spaxels at larger radii from the center of the galaxy will suffer from lower S/N than the central spaxels, so we bin them in order to measure kinematics at a consistent S/N and avoid introducing potential biases. We use the VORBIN[11] (M. Cappellari & Y. Copin 2003) Voronoi binning software to select only spaxels with an S/N (per angstrom) greater than one and group those spaxels to achieve close to a designated target S/N within each bin. An example of this selection for target S/N values of 10 and 20 is shown in Figure 2. For our baseline, we use an S/N target of 15, which results in roughly 50–100 spatial bins depending on the

[10] We used v9.0.1 of the Python package from https://pypi.org/project/ppxf.
[11] We use v3.1.5 of the Python package from https://pypi.org/project/vorbin.

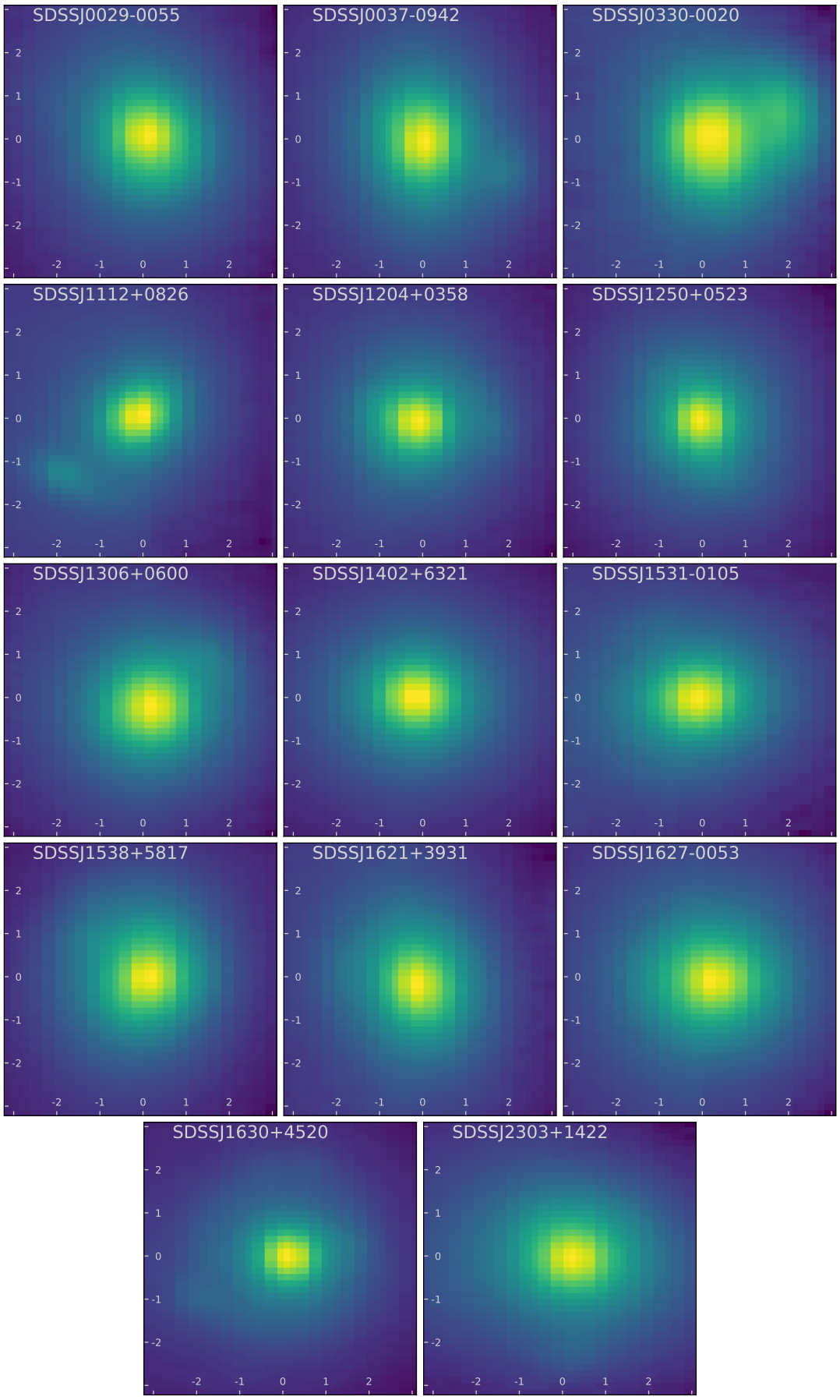

Figure 1. Data cube for each object summed across all wavelength bins in the fitted range 3600–4500 Å and cropped to 43 × 43 pixels (6.″235 × 6.″235).

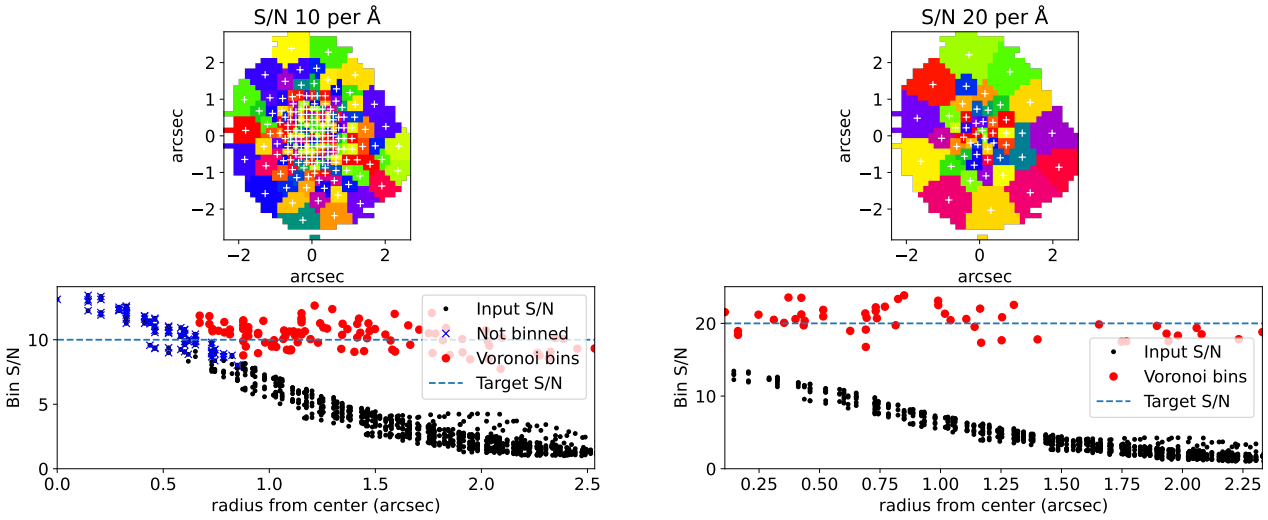

Figure 2. Voronoi binning of SDSS J0037−0942 with target bin S/N ratios of 10 (left) and 20 (right). The upper plot for each is a map showing the spatial boundaries of bins, with bin centers marked with "+." Beneath, we show the binning. The vertical axis is in units of S/N Å^{-1}, and the horizontal axis is the radius from the center. Black dots are the spaxels that are binned, and blue crosses indicate spaxels with a high enough S/N to be a bin on their own. Red markers are the Voronoi bins. Taking a lower target S/N offers more spatial information at the cost of increased uncertainty in the kinematics of individual bins.

brightness of the object. In order to avoid overfitting and introducing biases, we do not fit each Voronoi bin independently with freely weighted stellar templates. Instead we first create a global template from a high-S/N (typically ∼100 Å^{-1}) aperture-integrated spectrum extracted from the data cube within half the effective radius of the galaxy.

Following TDCOSMO-XIX, for our baseline model, we fit the aperture-integrated spectrum with linear combinations of stellar templates from the Indo-US library of empirical stellar templates[12] (F. Valdes et al. 2004) in the wavelength range of 3600–4500 Å. We include corrective additive and multiplicative polynomials of degree six and two, respectively, and convolve with a Gaussian (`moments = 2` in PPXF) LOSVD kernel. This linear combination of typically ∼20–30 stellar templates is the global template for fitting the spatial Voronoi bins of the data cube. Example global template spectra extracted from the centermost spaxels for each of the 14 objects are shown in Figure 3. The composite spectrum in each Voronoi bin is then fit with the appropriate annular global template with fixed template weights by scaling the overall normalization, introducing new corrective polynomials as described above, and convolving with an LOSVD. The extracted mean velocity is a small correction to the galaxy's cosmological recession velocity. Due to how the velocity is defined in PPXF, the peculiar velocity in the galaxy's rest frame can be obtained by simply subtracting the velocity of the barycenter from the fitted velocity (M. Cappellari 2023, Equation (3)). This gives the galaxy's rotation with positive values showing receding (redshifted) bins. The resulting kinematic maps describe the 2D projection of stellar motion within the galaxy.

This method assumes that the kinematic tracer population is adequately described by a single spatially uniform stellar population and is standard practice for extracting the kinematics of ETGs (see, e.g., K. Zhu et al. 2023). Following the methods outlined in TDCOSMO-XIX for evaluating the goodness of fit across several models by comparing the Bayesian information criterion (BIC; see TDCOSMO-XIX Section 5 and appendix for full derivations) for each model, we investigate the possibility of a radial stellar population gradient by fitting radial annuli instead of a single central aperture. We take annuli of radial width $= 0\farcs5$ centered at the brightest spaxel in the center of the deflector galaxy. We ensure the aperture-integrated spectra from annular bins have S/N > 30, but most are closer to 60–70. Voronoi bins are fit with the appropriate annular global template according to the radius of the luminosity-weighted center of the Voronoi bin. In this way, we allow for gradients in the stellar population while controlling for spurious individual bin fits. At the Voronoi bin level, compared with our baseline bin measurements (with a single global template), the flexible stellar population results in random variations to the extracted velocity dispersions at the 1% level that are highly correlated with the bin's membership in the annular bins. The resulting BIC evidence shows no indication of improved goodness of fit for the added flexibility, and there is a clear risk of introducing a systematic bias to the radial profiles of the velocity dispersions. Therefore, we utilize a single global template for each galaxy. We go into further detail regarding systematic effects in Section 3.1.

3.1. Systematics, Biases, and Error Budget

Formal statistical uncertainty estimates in the PPXF model are computed from the standard errors in the fit and are corrected by multiplying by $\sqrt{\chi^2}$, in order to account for potential error under-/overestimates. χ^2 is calculated as the square sum of the residuals between the model spectrum and data divided by the degrees of freedom (approximately the number of spectral bins). In order to test the robustness of the statistical uncertainties on the extracted bin kinematics, we use wild bootstrapping with a Rademacher distribution (see R. Davidson & E. Flachaire 2008, Equation (7)) of residuals for each bin fit for each object in our sample. Across all bins, the uncertainties on the mean velocity (velocity dispersion) from bootstrapping are on average 2.6% (3.1%) smaller than the PPXF formal uncertainties, with a standard deviation of 5.6% (5.3%). Similar tests were done with MaNGA data (see

[12] https://noirlab.edu/science/observing-noirlab/observing-kitt-peak/telescope-and-instrument-documentation/cflib

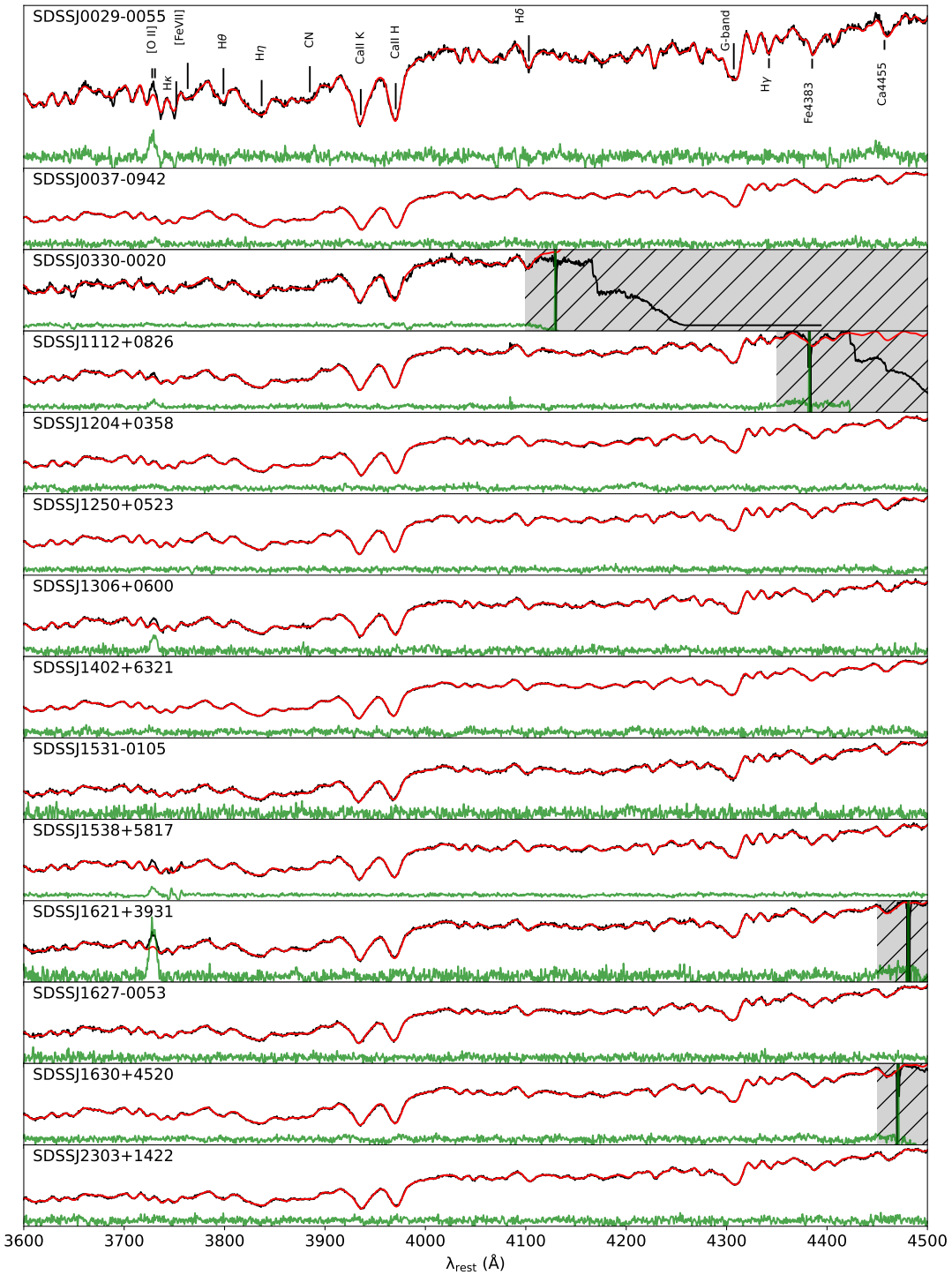

Figure 3. Rest-frame spectrum of each deflector galaxy in our sample extracted from an aperture of half the galaxy's effective radius, fit with stellar template spectra from the X-shooter Spectral Library (XSL). Black lines show the data. Red shows the model. Green shows rescaled residuals. Gray regions show masked wavelengths where the redshifted observed wavelengths are redder than the instrument range. Notable line features are highlighted in the first spectrum for demonstration. During fitting, sigma-clipping removes some contaminating emission lines, especially [O II] λ3727, and spurious single wavelength elements.

right panel of Figure 20 in K. B. Westfall et al. 2019), finding that the PPXF formal uncertainties are very close to the true ones, except at unreasonably low S/Ns. We therefore utilize and report the formal statistical uncertainties directly from PPXF.

With our state-of-the art methods and the high quality of KCWI data, the statistical errors at the Voronoi bin level are on average 3%–4%, which easily achieve the precision required for population-level inferences. However, potential sources of systematic error may bias individual measurements or introduce covariance at the bin or sample level, introducing an effective noise floor that is independent of sample size or S/N. Some well-studied sources of systematics include instrumental resolution, S/N, wavelength range, mismatch between templates and galaxy spectra, flux calibration, and interstellar absorption. Many excellent studies on this topic

have been published in the past (e.g., A. Dressler 1984; D. D. Kelson et al. 2000; T. Treu et al. 2001; A. J. Barth et al. 2002; C. Spiniello et al. 2015, 2021a, 2021b; G. D'Ago et al. 2023; K. Mehrgan et al. 2023). We experimented with a variety of additional potential sources of systematic uncertainty by testing small adjustments to virtually every step in our fitting procedure. Systematic choices that we tested and found to result in negligible differences include the degrees of corrective polynomials (0.6%), target S/N thresholds for Voronoi binning, subsets of stellar templates from within the same library, and masks over individual absorption features present in the wavelength range of fitting. Ultimately, we found that only two aspects made a difference beyond the 1% level in bin velocity dispersions: the library of stellar templates from which the galaxy spectra are fit and the wavelength range used.

To address the first, the TDCOSMO collaboration implemented a rigorous study of template libraries and our methods for extracting stellar kinematics (TDCOSMO-XIX). We demonstrated with four independent data sets (including the KCWI data presented here) and three independent code implementations that the most popularly used stellar template libraries are unbiased in velocity dispersion to a subpercent level when they are properly cleaned of contaminants and applied to appropriate wavelength ranges for data of high S/N. The libraries that were cleaned and examined were Indo-US, MILES[13] (P. Sánchez-Blázquez et al. 2006; J. Falcón-Barroso et al. 2011), and XSL[14] (K. Verro et al. 2022). For that analysis, the KCWI data cubes were integrated over a 1″ radius from the center of the galaxy in order to achieve an average S/N of 160 Å^{-1}, which reduces the statistical uncertainty well below the effects of systematics. We introduced a procedure to evaluate the evidence for each library based on the BIC measurement for each data set. The SLACS KCWI data set revealed a strong preference for the Indo-US stellar template library, with a negligible contribution to the systematic uncertainty when accounting for the BIC preference. We therefore take the Indo-US extractions as the fiducial models. When averaged over the sample, velocity dispersions measured with the MILES library are 0.7% ± 0.3% higher, and XSL results in velocity dispersions that are 1.0% ± 0.2% lower. Even when averaged with equal weight over the stellar template libraries, the systematic uncertainty is still subpercent at 0.79%. The stellar template libraries were constructed from observations with different instruments and different stars, so across a sample of galaxies, the measured velocity dispersions from one template library compared with another are correlated. Sample-level covariances are 0.47% when BIC weighted and 0.86% when averaged with equal weight over the stellar template libraries. We also included single stellar population models and found they lack the flexibility provided by individual stellar spectra. We do not recommend their use for subpercent accuracy. We also tested subsets of libraries selected at random or by stellar temperature and metallicity and found them to consistently recover the same sets of stellar templates and extracted kinematics, indicating that PPXF is able to efficiently select the most appropriate templates from a given library without a preselection based on assumptions about the stellar population. Given well-calibrated and appropriately representative empirically derived template libraries, and with careful selection of the wavelength range of the fit, the systematic effects from the template selection are well controlled.

The wavelength range specified for spectral fitting can introduce systematic effects in the selection of stellar templates and in the extracted bin kinematics. For example, the truncation of any line feature by wavelength boundaries (especially at the longer-wavelength end) can affect the fit. To mitigate this effect, we select bounds where the continuum is relatively flat and there are no contaminating spectral features. In addition, we find that fits suffer when including much of the rest-frame UV spectrum below 3600 Å. This is due to low S/N and poor flux calibration of the stellar libraries below this blue cutoff. Extending fits to bluer regions will require better stellar templates than the ones currently available. However, this is not an issue, since the complex spectrum there does not contain absorption features that are clearly informative for the stellar kinematics, and fits that include those wavelengths include large contributions from hot F, A, and B stars that may be thermally broadened and bias the velocity dispersion measurements.

We test three regions of equal wavelength range enclosed within our baseline extraction range: 3600–4250 Å, 3700–4350 Å, and 3800–4450 Å. Two of our galaxies (SDSS J0330-0020 and SDSS J1112+0826) are higher redshift than the others, and their rest-frame spectra do not span the full range of wavelengths needed for this test. We remove those two and test the systematics with the other 12 objects. Unlike the analysis presented by TDCOSMO-XIX, the wavelength effect on the extracted velocity dispersion cannot be assessed in terms of the BIC goodness of fit. This is because the BIC deals with the likelihood of the data given a systematic model choice. Comparing kinematic extractions of different ranges of spectra is by definition utilizing different data with different noise realizations. In order to get the closest possible comparison, we ensure that the variations in the wavelength ranges span the same number of sampled data points, which depends on the galaxy's redshift. Because the data are logarithmically rebinned before fitting, the wavelength ranges centered at longer wavelengths will have fewer sampled data points. We calculate the number of data points in the range 3600–4250 Å and extend the blue end of the other two ranges to include the same number of total sampled points. Because the noise realization is different for each range, the systematic effect is muddled by random noise variations, so we need to use the highest possible S/N. Following TDCOSMO-XIX, we integrate each data cube within 1″. At the sample level, the effect of one wavelength selection compared with another averages to zero. We create a 12 × 12 covariance matrix to quantify the covariance between objects. Matrix element (n, m) is calculated as

$$\Delta_{n,m} = \frac{\langle \Delta\sigma_{n,i} \Delta\sigma_{m,i} \rangle}{\bar{\sigma}_n \quad \bar{\sigma}_m}, \tag{1}$$

where

$$\Delta\sigma_{n,i} = \bar{\sigma}_n - \sigma_{n,i}, \tag{2}$$

and $\sigma_{n,i}$ is the velocity dispersion from the ith variation of object n.

The average of the diagonal is 0.8%, and the average off-diagonal is consistent with zero within the error on the mean. We test for spatial covariance by repeating the test at the bin level, creating an $N \times N$ covariance matrix for each object

[13] https://research.iac.es/proyecto/miles/
[14] http://xsl.u-strasbg.fr/

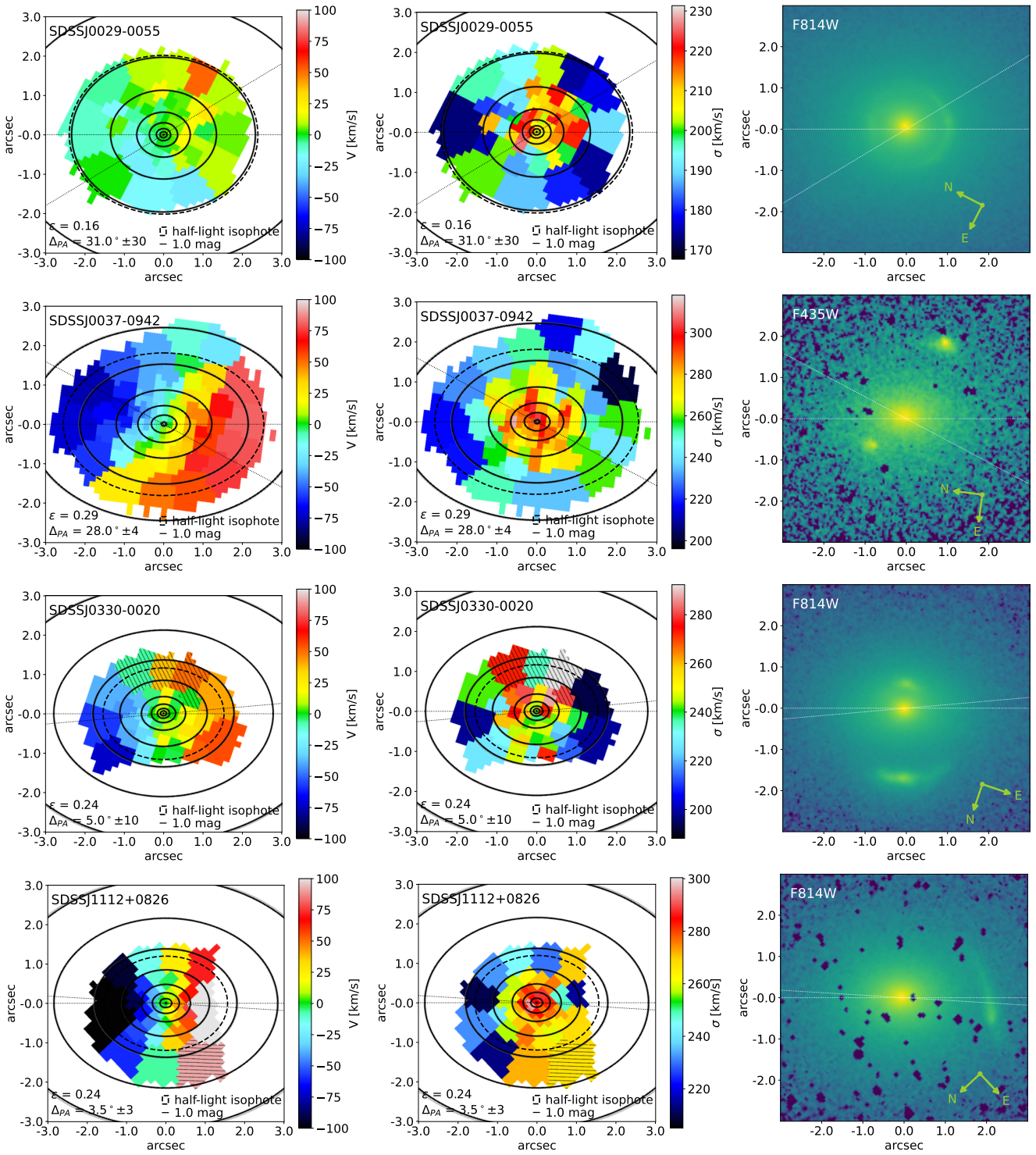

Figure 4. We show the kinematic maps of each object: mean velocity (left column) and velocity dispersion (middle column). We also show the available HST image closest in wavelength to KCWI (right column, F435W, F606W, or F814W). We scale mean velocities to 100 km s^{-1}. Velocity dispersions are shown in the range of the minimum and maximum value ($\pm$5 km s^{-1}) shown in the color bar to the right of each kinematic map. Red to white indicate the highest values (or receding velocity) and blue to black indicate the lowest values (or approaching velocity), with green indicating "zero" velocity or midpoint. Bins with random uncertainties $>$ 20 km s^{-1} are hashed. These bins often correspond to regions where the background source is significant, but we chose not to mask before fitting. We use MGEFIT to translate the B-spline surface brightness models of the foreground lens galaxy (with background source features subtracted) into multiple Gaussian components for use in dynamical modeling. Surface brightness contours are overlaid on the kinematic maps. Dark contours indicate the best-fit MGE solution to the gray B-spline model surface brightness. Images are oriented so that the photometric major axis is aligned horizontally. This axis is shown with a dotted line, in addition to a second dotted line showing the kinematic axis. The lower left details the best-fit ellipticity from the MGE translation of the B-spline models and the misalignment of the kinematic and photometric axes. For some objects, the misalignment shown here is insignificant because of the high uncertainty in the determination of the kinematic axis or very round isophotes. Arrows indicating north and east are placed in the HST images in the right column.

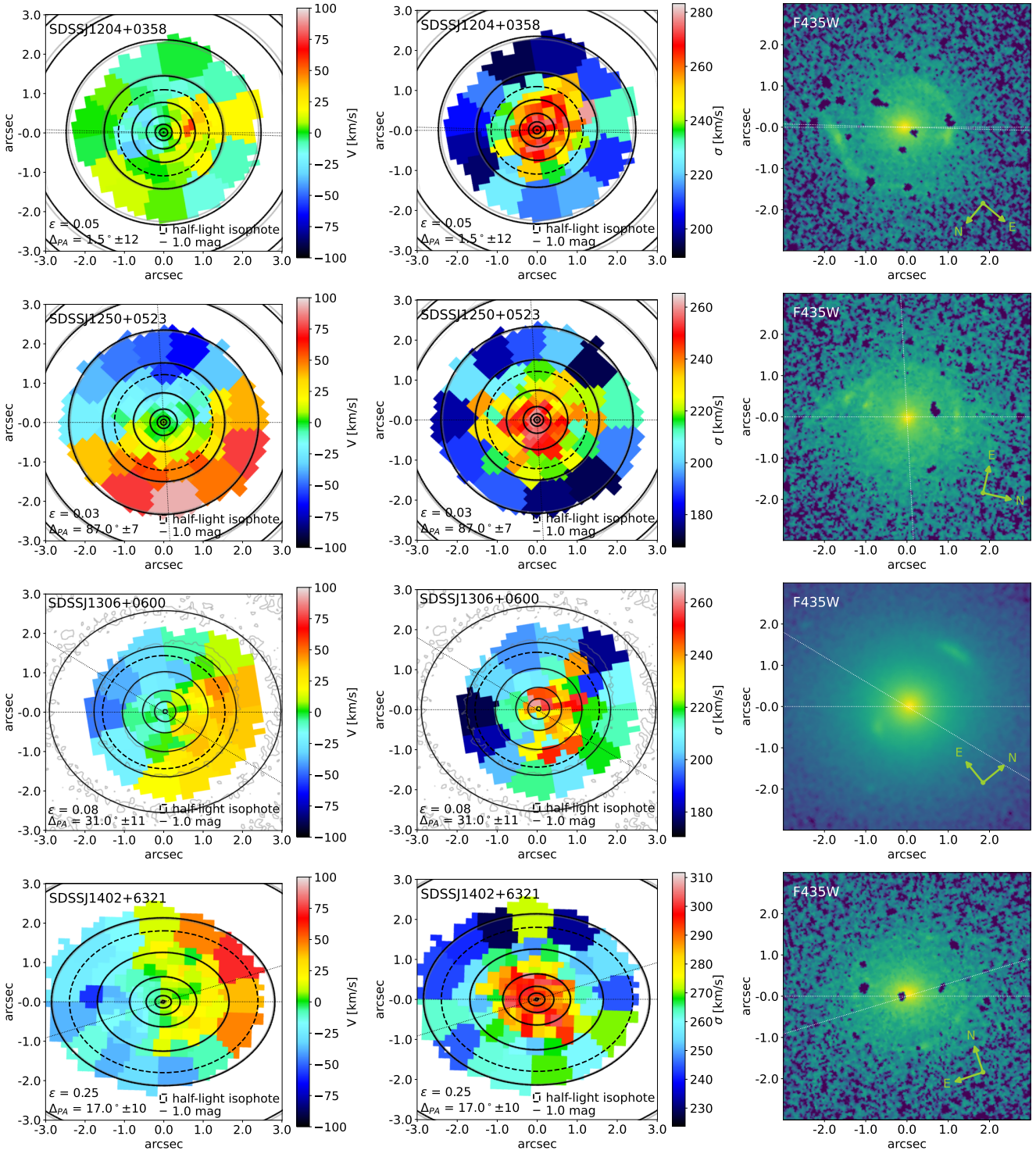

Figure 4. (Continued.)

where N is the number of spatial bins. We then average over each object and then over the sample to quantify the average contribution to the bin variance. We test increasing S/N of the spatial Voronoi bins and find the average diagonal and off-diagonal terms are consistently at the noise level, approaching 1% for both the diagonal and off-diagonal terms for bins with an S/N of 60 $Å^{-1}$. This suggests that the contribution of the wavelength effect to the error budget is <1% and the bin covariance is mostly due to the residual noise.

The subpercent covariance from both the template and wavelength contributions results in a total systematic component per object in the range 1%–1.4% and a subpercent covariance. It is thus sufficient to improve our hierarchical inference of the Hubble constant to 2% with the addition of more SLACS lenses to the external population of non-time-delay lenses alone (given equivalent data to this sample). Improved kinematic data sets reaching further in the red, with reduced sensitivity to templates (A. J. Barth et al. 2002),

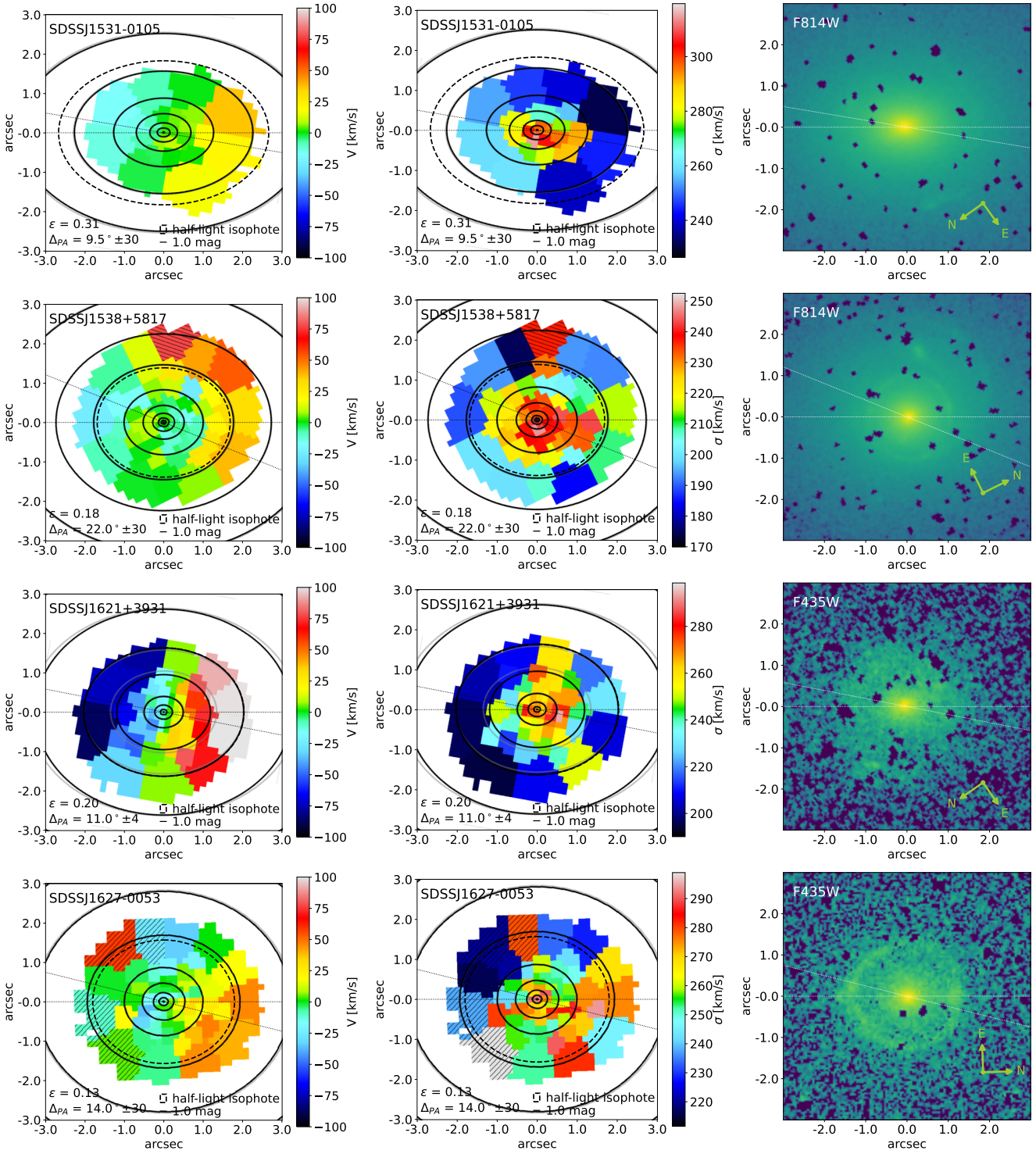

Figure 4. (Continued.)

e.g., with the new KCRM red arm of KCWI, or with NIRSPec on JWST, are needed to further reduce these covariances and their effects on cosmological inferences.

3.2. Contamination from Background Source

For 12 of the 14 objects, the lensed background source arcs are faint enough that we are able to extract from spatial bins even with some contamination from the lensed arcs. We note that several of these bins have higher uncertainty in the extracted kinematics than bins that are farther from the lensed arcs. We retain those bins and flag those with uncertainty in the velocity dispersion greater than 20 km s^{-1}. In two cases, SDSS J0330−0020 and SDSS J1112+0826, the background source at higher redshift is bright enough to significantly affect the Voronoi binning and the extraction of kinematics from bins

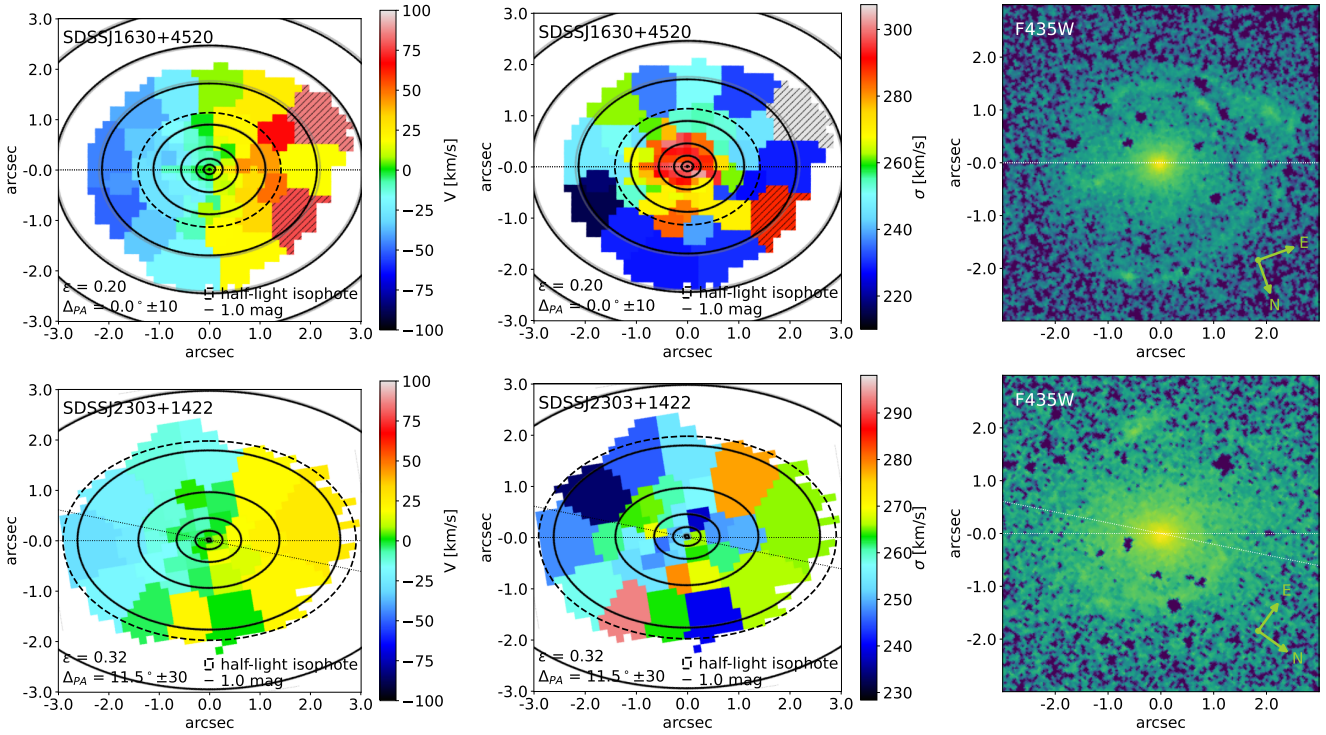

Figure 4. (Continued.)

that include contaminated spaxels. For these objects, we mask these pixels by eye and fit as above. We tested two methods for iteratively fitting the foreground and background galaxy spectra. We fit composite spectra taken from spaxels at the center of the object and from the region most contaminated by the background source arc. Initially, we used a technique similar to the method used in TDCOSMO-XII to remove contaminating background quasar continuum spectra using KCWI data. We take the extracted background source spectrum from the data as a template for fitting the contamination in other spatial bins. The background source galaxy arcs in our data are not bright enough relative to the foreground deflector for a clean separation of the light; the deflector CaHK absorption features are clearly present in the template constructed from the extracted background source arc. To improve on this, we simultaneously fit both spectra extracted from the foreground and background components with the same stellar template library at the rest frame of the foreground deflector. We redshift the templates to the appropriate redshift for the background galaxy relative to the rest frame of the foreground deflector. Then we alternately fit the extracted central spectrum and background source spectrum to iteratively improve both fits. The result still does not cleanly separate the foreground and background source light, so we opt to mask the most affected spaxels and extract kinematics where there is no contamination. This method will be useful for future IFS data sets of strong lenses, e.g., with JWST, where the sensitivity and resolution will allow cleaner separation of the background source spectral features.

4. Results

We present the final kinematic maps and HST photometry in Figure 4. The following subsections discuss kinematic classification and integrated kinematics. We present some select details in Table 2.

4.1. Kinematic Classification

Hints of a distinction between the two main classes of ETGs were evident even before spatially resolved kinematics were possible, when velocities much lower than theoretical predictions were measured in the first single-aperture stellar kinematic observations of ETGs (F. Bertola & M. Capaccioli 1975; G. Illingworth 1977; J. Binney 1978). This challenged the assumption that ETGs are universally homogeneous isotropic systems. To quantify this, J. Binney (1978) introduced the $(V/\sigma, \epsilon)$ diagram. V/σ is the ratio of rotational to "random" velocity integrated spatially across the galaxy, and ϵ is the observed ellipticity of the galaxy. This can be extended to spatially resolved kinematics by taking the flux-weighted (F_p) average of velocities V_p and σ_p of the pth pixel replicated from the kinematics of the bin to which pixel p belongs (M. Cappellari et al. 2007; M. T. Graham et al. 2018):

$$\frac{\langle V^2 \rangle}{\langle \sigma^2 \rangle} \approx \left(\frac{V}{\sigma}\right)_e^2 \equiv \frac{\sum_p F_p V_p^2}{\sum_p F_p \sigma_p^2},$$

summing over all pixels inside the effective radius of the galaxy. V/σ contains no spatial information, so E. Emsellem et al. (2007) introduced another quantitative kinematic description with a proxy for angular momentum $\boldsymbol{L} = \langle \boldsymbol{R}|\boldsymbol{V}| \rangle$, normalizing it with the rms velocity $V_{\rm rms} = \sqrt{V^2 + \sigma^2}$. With R_p the position of pixel p, we get

$$\lambda_{\rm R} \equiv \frac{\langle R|V| \rangle}{\langle R\sqrt{V^2 + \sigma^2} \rangle} = \frac{\sum_p F_p R_p |V_p|}{\sum_p F_p R_p \sqrt{V_p^2 + \sigma_p^2}}.$$

Table 2
Kinematic Details for the 14 SLACS Lenses

Object	$z_{\rm lens}$	$\sigma_{1/2}^{\rm KCWI}$ (km s^{-1})	$\sigma_{\rm eff}^{\rm KCWI}$ (km s^{-1})	$\sigma_{1.5}^{\rm KCWI}$ (km s^{-1})	$\sigma_{\rm SDSS}^{\rm this\ work}$ (km s^{-1})	$\sigma_{\rm XII}^{\rm SLACS}$ (km s^{-1})	$\sigma_{\rm IX}^{\rm SLACS}$ (km s^{-1})	$R_{\rm eff}$ (arcsec)	$\epsilon_{\rm obs}$	V/σ	λ_R	Class
SDSS J002907.77-005550.5	0.227	207 ± 7	200 ± 9	206 ± 2	197 ± 18	216 ± 15	229 ± 18	2.30	0.16	0.070	0.056	slow
SDSS J003753.21-094220.1	0.195	279 ± 7	265 ± 8	274 ± 1	309 ± 14	265 ± 8	279 ± 10	2.30	0.27	0.162	0.151	slow
SDSS J033012.14-002051.9	0.351	258 ± 12	247 ± 13	250 ± 5	288 ± 26	273 ± 23	212 ± 21	1.26	0.23	0.106	0.094	slow
SDSS J111250.60+082610.4	0.273	274 ± 7	264 ± 9	270 ± 2	271 ± 22	260 ± 15	320 ± 20	1.55	0.23	0.236	0.208	fast
SDSS J120444.07+035806.4	0.164	262 ± 5	249 ± 7	246 ± 2	254 ± 18	251 ± 12	267 ± 17	1.63	0.03	0.071	0.059	slow
SDSS J125028.26+052349.1	0.232	243 ± 6	231 ± 7	235 ± 1	220 ± 12	242 ± 10	252 ± 14	1.86	0.03	0.129	0.113	fast
SDSS J130613.65+060022.1	0.173	230 ± 7	221 ± 9	223 ± 2	242 ± 18	248 ± 14	237 ± 17	2.08	0.09	0.110	0.101	slow
SDSS J140228.21+632133.5	0.205	285 ± 7	276 ± 8	279 ± 1	249 ± 14	274 ± 11	267 ± 17	2.65	0.23	0.084	0.073	slow
SDSS J153150.07-010545.7	0.160	273 ± 9	267 ± 10	272 ± 2	262 ± 13	261 ± 10	279 ± 12	2.73	0.32	0.052	0.045	slow
SDSS J153812.92+581709.8	0.143	236 ± 5	225 ± 7	216 ± 2	[a]	177 ± 9	189 ± 12	1.45	0.18	0.055	0.048	slow
SDSS J162132.99+393144.6	0.245	255 ± 10	242 ± 12	256 ± 2	238 ± 21	234 ± 15	236 ± 20	2.30	0.27	0.224	0.200	fast
SDSS J162746.45-005357.6	0.208	262 ± 10	261 ± 12	261 ± 2	254 ± 13	274 ± 11	290 ± 14	2.02	0.15	0.083	0.070	slow
SDSS J163028.16+452036.3	0.248	280 ± 7	267 ± 9	271 ± 2	269 ± 16	283 ± 13	276 ± 16	2.01	0.16	0.095	0.088	slow
SDSS J230321.72+142217.9	0.155	259 ± 9	258 ± 9[b]	257 ± 2	267 ± 21	251 ± 13	255 ± 16	3.46	0.36	0.062	0.058	slow

Notes. KCWI velocity dispersions have all been extracted with the Indo-US library. $\sigma_{1/2}^{\rm KCWI}$ and $\sigma_{\rm eff}^{\rm KCWI}$ are the KCWI velocity dispersion within $1/2$ $R_{\rm eff}$ and 1 $R_{\rm eff}$, respectively, measured by luminosity-weighted integration over the 2D velocity dispersion map. $\sigma_{1.5}^{\rm KCWI}$ is the KCWI velocity dispersion extracted from the data cube integrated over an aperture of $1\farcs5$ with mock SDSS seeing. $\sigma_{\rm SDSS}^{\rm this\ work}$ is the velocity dispersion measured from SDSS spectra using XSL stellar templates in this work. $\sigma_{\rm XII}^{\rm SLACS}$ is measured from SDSS spectra by Y. Shu et al. (2015). $\sigma_{\rm IX}^{\rm SLACS}$ is measured from SDSS spectra in SLACS-IX. Errors quoted here are statistical errors. The effective radius $R_{\rm eff}$ is reported from SLACS-X. Observed ellipticity $\epsilon_{\rm obs}$ is measured from MGE models at the isophote enclosing half the total luminosity. V/σ, λ_R, and kinematic classification are defined in Section 4.1.

[a] SDSS J1538+5817 has two SDSS observations in the SDSS Science Archive Server (SAS). We measured both with pPXF and report both. One yields 180 ± 12 km s^{-1}, which closely agrees with SLACS-IX and SLACS-XII values. The other yields 253 ± 15 km s^{-1}. The value we measure over the same aperture with KCWI data and mock seeing, 216 ± 2 km s^{-1}, is at the midpoint between these two values.

[b] SDSS J2303+1422's large effective radius is beyond the size of the kinematic map. We report the value integrated over the whole map.

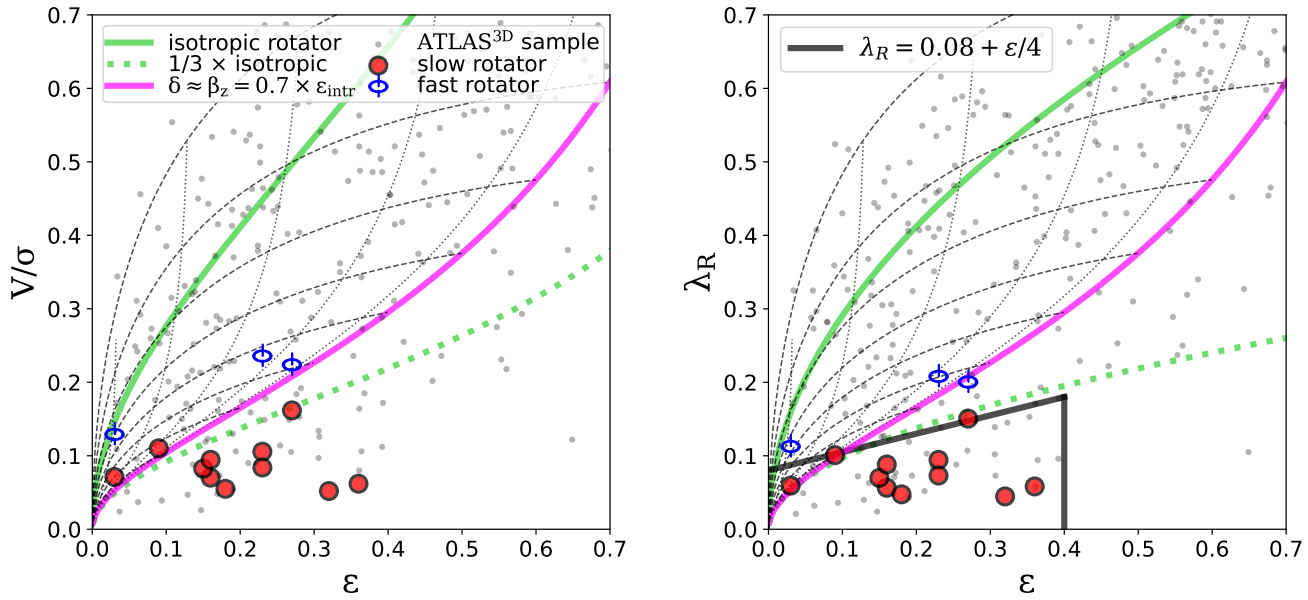

Figure 5. We plot $(V/\sigma, \epsilon)$ (left) and (λ_R, ϵ) (right) calculated for each of our 14 SLACS lenses. See Section 4.1. ϵ is the observed ellipticity, measured from the MGE models at the isophote enclosing half the total luminosity. V/σ and λ_R are calculated from the kinematic maps integrated within the circularized rest-frame-corrected V-band effective radius as reported in SLACS-X. The solid green curve shows the theoretical values for a perfectly isotropic galaxy seen edge on (J. Binney 2005), and the dotted green line shows one-third of that value, which has been shown to roughly approximate the separation of fast/slow rotators on the $(V/\sigma, \epsilon)$ diagram for nearby ETGs (M. Cappellari 2016). The magenta curve shows the edge-on relation $\delta \approx \beta_z = 0.7 \times \epsilon_{\rm intr}$ from M. Cappellari et al. (2007). Dotted lines are the same relation projected at different inclinations at intervals of 10°, and dashed lines are contours of equal intrinsic ellipticity for the relation at different projections. Fast rotators are consistent with being randomly oriented oblate axisymmetric galaxies with anisotropy $\beta \leqslant 0.7$ (i.e., they lie above the magenta curve). In the right plot, the black lines show selection criteria $\lambda_R < 0.08 + \epsilon/0.4$ and $\epsilon < 0.4$ (Equation (19) of M. Cappellari 2016), which have been shown to reliably separate fast and slow rotators as well. Gray scatter markers indicate the ATLAS^{3D} sample. Blue and red markers respectively indicate quantitative classification as fast and slow rotators as reported in Table 2.

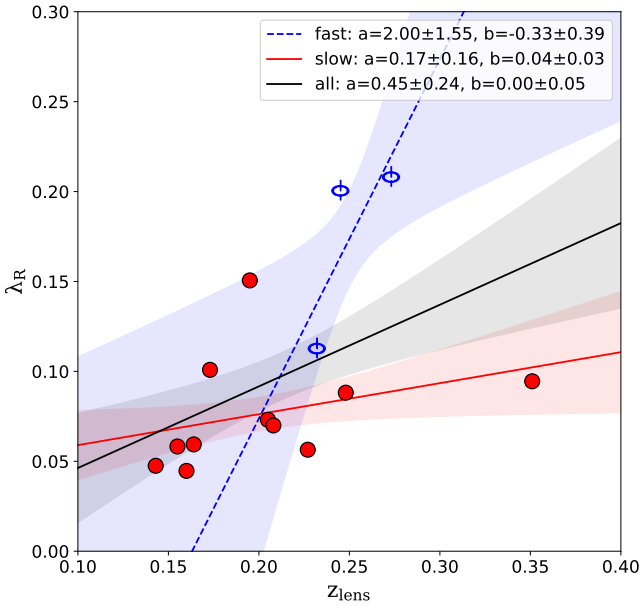

Figure 6. λ_R as a function of lens redshift. Markers show the objects' classification as fast/slow rotators, as given in Table 2. The dotted blue line is fit to fast rotators. The solid red line is fit to slow rotators. The solid black line fits all objects.

Values of V/σ and λ_R plotted against ϵ for the 14 objects are shown in Figure 5 and listed in Table 2.

The green curve in both plots of Figure 5 shows the theoretical V/σ values for a perfectly isotropic system with given ellipticity (see Equation (26) in J. Binney 2005); here $\alpha = 0.15$ as in M. Cappellari et al. (2007). A dividing line between fast and slow rotators can be taken as the curve delineating one-third of this value (see, e.g., M. Cappellari 2016, Section 3.5.3). SAURON, ATLAS^{3D}, etc., were analyzed in this way, and the data pointed to a stronger separating feature set (E. Emsellem et al. 2011). A dividing region of low rotation and low ellipticities defined by $\lambda_R < 0.08 + \epsilon/0.4$ and $\epsilon < 0.4$ (Equation (19) in M. Cappellari 2016) reliably separates fast and slow rotators from those data sets. These classifications are useful for characterizing these systems in the context of more detailed studies of nearby galaxies.

We are able to detect rotation in all mean velocity maps. O. Czoske et al. (2012) found evidence for rotation in about one-third of their sample of 17 SLACS lenses (many of which are also in our sample), which demonstrates the quality of the KCWI data. Despite the detectability of rotational velocity, 11 of the 14 SLACS lenses are quantitatively slow/nonregular rotators when plotted in comparison to SAURON and ATLAS^{3D} samples on the $(V/\sigma, \epsilon)$ and (λ_R, ϵ) diagrams (see Figure 5). For some objects, rotational velocities that reach $\sim$100 km s^{-1} are suppressed in the V/σ contest by velocity dispersions in the 300 km s^{-1} range. This is what we expect for our sample of very large ETGs in the range $\sim 10^{11}$–$10^{12}\, M_\odot$, which are expected to be representative of the population that likely formed from multiple dry mergers. However, several of them have significant enough rotation that they may need to be accounted for during dynamical modeling, in order to constrain the dynamical mass models at the few-percent level needed for precision cosmology. We leave this analysis for follow-up work (S. Knabel et al. 2025, in preparation). When it matters, we rely primarily upon the (λ_R, ϵ) to guide our classification, and we report our overall classifications in Table 2.

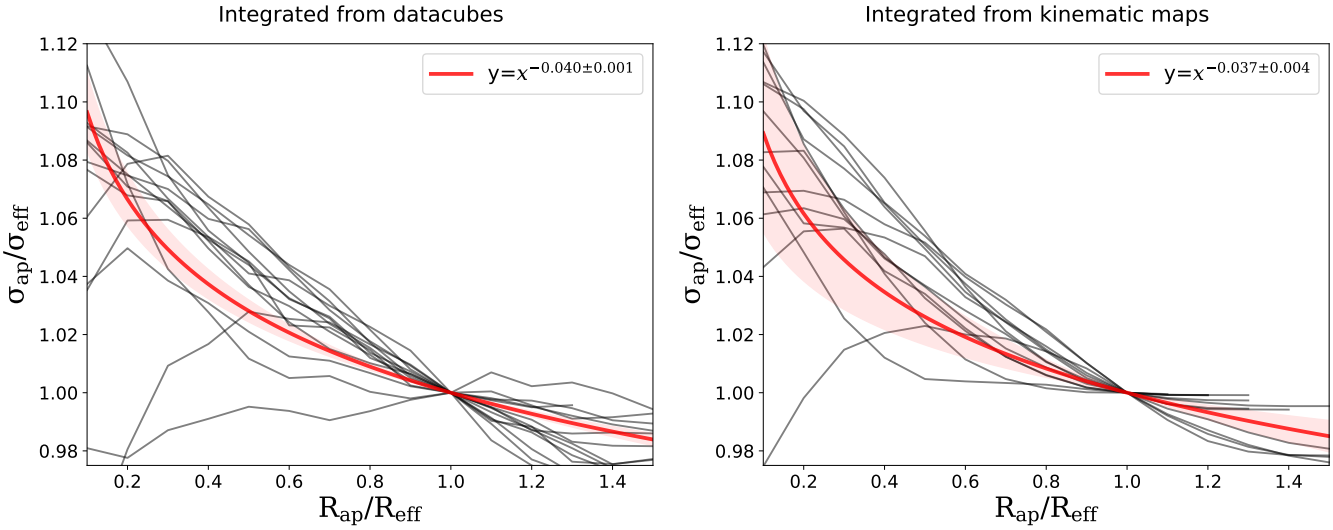

Figure 7. Tests of aperture-correction formulas. The y-axis shows the aperture-integrated velocity dispersions calculated by luminosity-weighted integration of the kinematic maps. The x-axis shows the radius of integration. Both are normalized to the rest-frame *V*-band effective radius as in SLACS-X. The red line shows the mean power-law fits for 13 of the 14 objects (shown in gray). SDSS J2303+1422 has a very large effective radius that is not reached by the kinematic maps. We therefore do not include this object in the average.

In Figure 6, we show λ_R as a function of redshift, respectively distinguishing the fast and slow rotators with blue and red markers as in Figure 5. The blue dotted line is fit to the fast rotators, and the red solid line is fit to the slow rotators. The data hint at an increase in λ_R with redshift for both classes. The extension to higher redshift of λ_R kinematic classification schemes derived from higher-resolution kinematics of more nearby surveys (e.g., SAURON, ATLAS^{3D}, and SAMI, J. van de Sande et al. 2017; SDSS MaNGA, M. T. Graham et al. 2018; CALIFA, J. Falcón-Barroso et al. 2019) is not foolproof. MaNGA observations (J. E. Greene et al. 2017; D. Bevacqua et al. 2022) have shown a number of visually "misclassified" fast rotators falling in the slow rotators zone in the (λ_R, ϵ) diagram, which could be an effect of low spatial resolution at higher redshifts than, e.g., SAURON observations. Even with the quality of the KCWI spatially resolved kinematics, it is difficult to parse out this effect until a larger representative sample is observed. The dominance of slow rotators in our sample is expected because the lensing cross section scales with σ^4, which favors the inclusion in lens samples of higher masses and velocity dispersions with respect to the general population of ETGs.

4.2. Integrated Velocity Dispersions, Aperture Effects, and Comparison with SDSS

Velocity dispersions obtained with single-aperture spectroscopy (hereafter "integrated kinematics") have limitations when compared to spatially resolved kinematics, but they are still extremely useful and will continue to be so for many applications. Very distant and compact sources, large spectroscopic surveys, multi-object spectroscopy (e.g., MOSFIRE; I. S. McLean et al. 2010, 2012), and studies of archival data (e.g., SDSS, etc.) will still provide compelling data. Inferences based on observed integrated kinematics have established and expanded our understanding of galaxy properties and scaling relations. In the context of time-delay cosmography, integrated kinematics are still constraining (though less so) for constraining the Hubble constant. For all of these reasons, it is worth comparing the KCWI kinematic maps with the SLACS-XII SDSS kinematics that are used in the hierarchical inference of TDCOSMO-IV.

Single-aperture velocity dispersion measurements are influenced by the size of the spectroscopic aperture. This effect cannot be fully decoupled from other instrument-specific effects, but spatially resolved kinematics allow us to examine the effects of integrating the velocity maps within various "aperture" sizes. The projected velocity dispersion profile of ETGs decreases with angular radius because the intrinsic orbital velocities generally decrease with radius from the center of the gravitational potential. This means a smaller aperture will generally measure a higher integrated velocity dispersion, as a result of varying anisotropy and the intrinsic mass density profile. Inclination effects can also influence integrated velocity dispersions. The interpretation of velocity dispersions reported in the literature is highly dependent on their definition and the specifics of the instrument and situation. This problem has been tested in V. N. Bennert et al. (2015) and shown to introduce up to 30%–40% differences between different definitions (inclination corrections and aperture sizes). Dynamical inferences from integrated kinematics (e.g., virial mass estimates) require relating the aperture to a more physical radius of the galaxy (e.g., the galaxy effective radius or half thereof).

To extract an integrated velocity dispersion for each object, we define a circular aperture centered on the lens galaxy center and integrate over all spaxels within that radius. We integrate within these apertures at the data cube level before fitting the 1D composite spectra as in the first step of our full kinematic extraction described in Section 3. As an additional test, we also extract a luminosity-weighted integrated velocity from the 2D binned kinematic map within the same radii (as in Sections 4.1 and 5). These two methods are consistent to 1% on average.

We look further at the effect of the integration aperture radius on the integrated velocity dispersion. A relation of $\sigma_{ap}/\sigma_{eff} \sim (R_{ap}/R_{eff})^{\eta}$, with $\eta \sim -0.06$–0.04 has been suggested in the literature for ETGs: e.g., -0.04 (I. Jorgensen et al. 1996), -0.06 (D. Mehlert et al. 2003), -0.066 (M. Cappellari et al. 2006), and -0.05 (Y. Shu et al. 2015). These relations can

Table 3
Uncertainties, as in Table 2 of TDCOSMO-XIX

Sample	$\langle \delta\bar{\sigma}/\bar{\sigma} \rangle$	$\langle \Delta\bar{\sigma}/\bar{\sigma} \rangle$	$\sqrt{\langle C_{i,j}\bar{\sigma}/\bar{\sigma}_i\bar{\sigma}_j \rangle_{i\neq j}}$	$\langle \Delta_B\bar{\sigma}/\bar{\sigma} \rangle$	$\sqrt{\langle C_{B,i,j}\bar{\sigma}/\bar{\sigma}_i\bar{\sigma}_j \rangle_{i\neq j}}$	Median S/N	No. Objects
KCWI	0.90%	0.79%	0.70%	0.97%	0.86%	153.6	14
SDSS S/N > 15	3.30%	1.39%	1.15%	1.70%	1.40%	17.3	38
SDSS S/N = (10, 15]	5.30%	1.88%	1.31%	2.30%	1.61%	11.7	98
SDSS S/N = [5,10]	7.71%	2.70%	1.86%	3.31%	2.28%	8.1	151

Note. For each data set, we report the average statistical error, the average systematic uncertainty associated with the choice of clean template library, the average amplitude of the off-diagonal terms of the covariance matrix between elements of the sample, the Bessel-corrected average systematic uncertainty, and the off-diagonal covariance matrix. Averages are calculated with equal weights, as in the lower panel of Table 2 of TDCOSMO-XIX. The KCWI values are identical to those found by TDCOSMO-XIX. The SDSS spectra have been separated into bins of S/N per angstrom, calculated in the range 4000–5000 Å.

be utilized to "correct" for aperture-size effects when comparing data collected within different aperture sizes. Figure 7 shows aperture-integrated velocity dispersions for each object integrated within radii in steps of 0.1× the rest-frame *V*-band effective radius as reported in SLACS-X, shown as gray curves, normalized by the velocity dispersion integrated within the effective radius. The left panel displays velocity dispersions from spectra integrated at the data cube level, while the right panel shows flux-weighted integrated velocity dispersions from the 2D binned kinematic maps. We fit the curve for each galaxy with a simple power law weighted by the inverse variance of the integrated velocity dispersions. For velocity dispersions integrated from data cubes and kinematic maps, respectively, we find $\eta = -0.040 \pm 0.001$ and $\eta = -0.037 \pm 0.004$. A weighted linear regression in log–log space closely agrees. This mean power-law fit is the red curve of both panels. We use $\eta = -0.040$ in the analysis of scaling relations in Section 5.1.

4.2.1. Our Method Applied to SDSS Spectra

We use our method to extract new velocity dispersions from SDSS spectra for the SLACS sample and compare with our KCWI measurements for the 14 galaxies of our sample, finding agreement between the data sets within the uncertainties, which are dominated by the lower S/Ns of the SDSS spectra. We retrieved the SDSS fiber spectra from SDSS DR17 (Abdurro'uf et al. 2022) via the SDSS Science Archive Server (SAS) and measured the spectra using PPXF for the 341 ETGS from the SLACS candidate parent sample. Where possible, we queried the same fiber spectra used for the SLACS-XII velocity dispersions. TDCOSMO-XIX used only the highest-S/N spectra (>15 $Å^{-1}$ from this sample) to test for systematic uncertainties as a result of stellar template library selection, finding systematic uncertainties of less than 2% and a strong preference for the XSL stellar library by BIC evidence. We extend that analysis using the same three cleaned stellar libraries (Indo-US, MILES, and XSL) to lower-S/N spectra and measure stellar library systematics for S/N bins of 5–10 and 10–15 $Å^{-1}$. Table 3 shows the average uncertainties over the SDSS S/N bin samples and the KCWI data for reference, as in the lower section of Table 2 in TDCOSMO-XIX. For very low-S/N spectra, the fits result in high statistical uncertainties $\langle \delta\bar{\sigma}/\bar{\sigma} \rangle$, making the data much more sensitive to changes in stellar libraries or other factors, enhancing the systematic errors. Furthermore, the BICs for the template libraries become completely indistinguishable. The SDSS data for the 14 KCWI objects have a mean S/N per angstrom of ∼9, and a maximum of 13. In Table 3, the bottom row has S/Ns in the range 5–10 with a median of 8.1, and it encompasses 10 of the 14 galaxies. The larger sample of SDSS spectra at these S/Ns resulted in an average statistical uncertainty of 7.7%, which is far above the systematic uncertainties attributable to template libraries that we find for any of the subsamples. For these reasons, we derive the systematic uncertainties for the purposes of this paper with equal weights to the three libraries instead of using BIC weighting. With a Bessel correction to account for the small number of libraries (see Equations (14)–(16) and Appendix A of TDCOSMO-XIX) the average systematic uncertainties for the bin with S/N in the range 5–10 are 3.31% in the diagonal and 2.28% in the off-diagonal. The off-diagonal represents the correlated effect of the differences in the stellar template libraries across a sample of measured velocity dispersions. In other words, changing from one library to another moves all the velocity dispersions up or down, in a coherent fashion, introducing covariance across the sample. For the bin with S/N in the range 10–15, the systematics are 2.30% and 1.61% in the diagonal and off-diagonal, respectively.

We extract kinematics from the KCWI data cube integrated within the 1.″5 SDSS aperture for comparison with the results from SDSS spectra. Typical seeing for our Keck observations is significantly better (FWHM ∼ 0.″8–0.″9) than that of the SDSS observations (FWHM ∼ 2″). PSF blurring tends to lower the integrated velocity dispersions as it introduces light from outer regions of the galaxy where the velocity dispersions are typically lower than in the central regions. We simulate the effect of the seeing difference by convolving the data cube with a Gaussian kernel when performing the aperture integration before kinematic extraction. We tested the dependence of the extracted velocity dispersions on the assumed seeing of SDSS observations by fitting with SDSS seeing of FWHM = 1.″5 and 2.″5, resulting in 0.58% ± 0.26% larger and 0.21% ± 0.25% smaller velocity dispersions, respectively. These are completely consistent within the statistical errors. Because the seeing FWHM for the Keck observations is much smaller, the effect is negligible. In Figure 8, we show the SDSS spectra in comparison with the KCWI spectra integrated within the same 1.″5 aperture. The average S/N per angstrom of the SDSS spectra for the 14 galaxies of this sample is ∼9, where the systematics in Table 3 are ∼3%. The average S/N of the KCWI sample is more than 1 order of magnitude higher.

The KCWI sample shows a strong BIC preference for Indo-US over MILES (greater than 6σ) and over XSL (at 3σ). The uncertainty on the difference in BIC between two libraries is estimated by bootstrapping over the 14 galaxies' fits and constructing a distribution of the difference in total BIC values

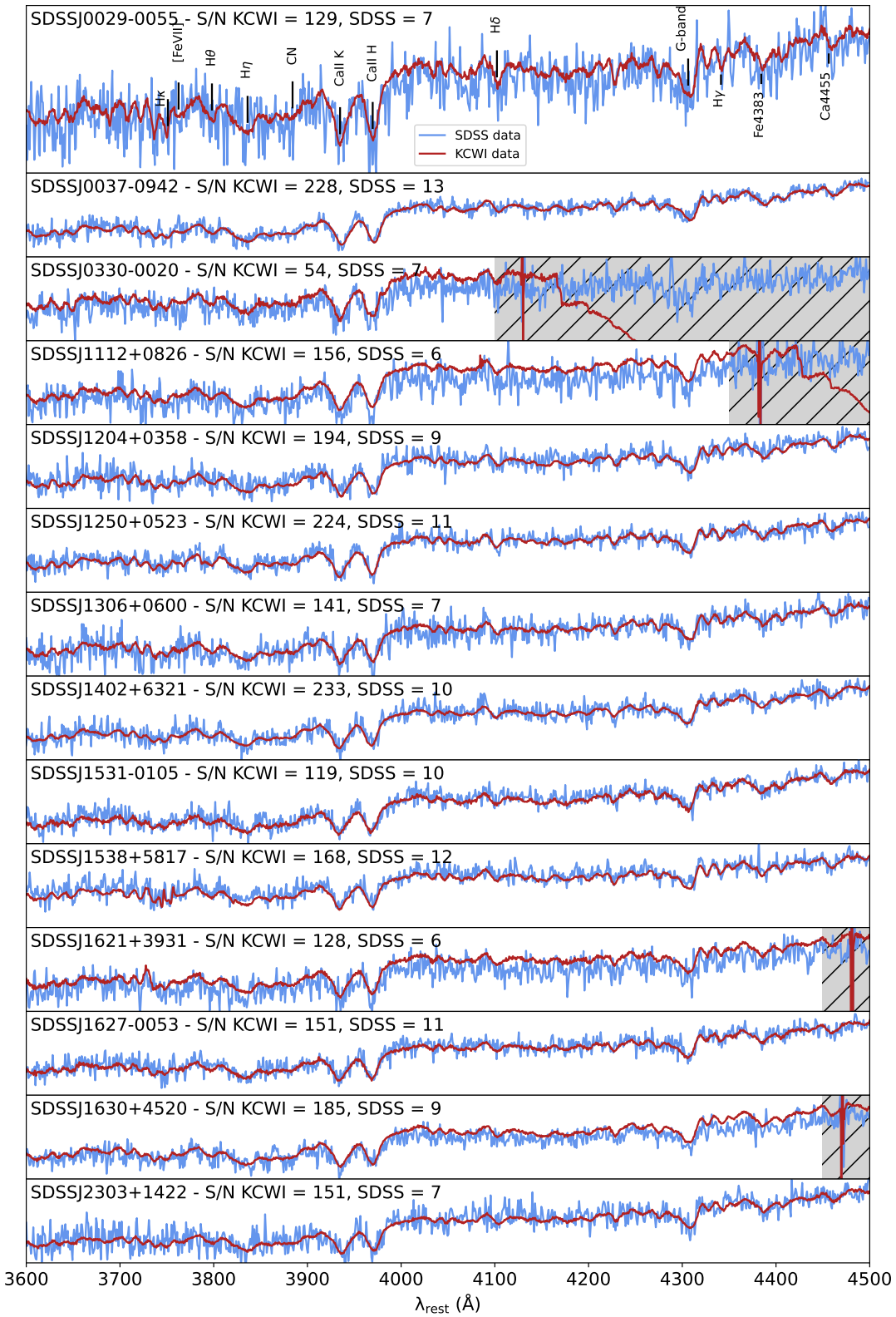

Figure 8. Rest-frame spectrum of each deflector galaxy in our sample. Red shows the KCWI data extracted from an aperture of the SDSS fiber size (1.″5). Blue shows the SDSS spectrum for the object. We list the S/N per angstrom for each spectrum measured in the range 4000–4500 Å. SDSS J1538+5817 has two fiber observations that conflict in extracted velocity dispersions. Here we show the fiber measured in SLACS-XII.

calculated from the combined number of parameters, number of data points, and likelihoods of each bootstrapped sample (see Section 5 of TDCOSMO-XIX for more details). The highest-S/N subsample of SLACS SDSS spectra with S/N > 15 Å^{-1} strongly prefers the XSL library over the Indo-US and MILES libraries (both at around 5σ). For all following comparisons, as well as comparisons with other analyses of SDSS data in Section 4.2.2, we take the BIC-preferred library

Table 4
Estimates of the Residual Uncertainties and Biases of Our SDSS Velocity Dispersions

Equation	Parameter	Best BIC	Indo-US	MILES	XSL
4	γ	$0.097^{+0.189}_{-0.075}$	$0.041^{+0.094}_{-0.026}$	$0.152^{+0.199}_{-0.121}$	$0.090^{+0.185}_{-0.069}$
	β	1.002 ± 0.020	1.008 ± 0.019	0.957 ± 0.020	0.993 ± 0.020
5	γ_*	$0.039^{+0.027}_{-0.021}$	$0.020^{+0.017}_{-0.007}$	$0.050^{+0.027}_{-0.024}$	$0.037^{+0.028}_{-0.020}$
	β	1.002 ± 0.022	1.006 ± 0.020	0.959 ± 0.023	0.993 ± 0.022

Note. We compare velocity dispersions extracted from SDSS spectra with our methods in comparison with KCWI aperture-integrated velocity dispersions with mock SDSS seeing, as in Equations (3)–(5). We compare the best-BIC libraries for each data set (Indo-US for KCWI and XSL for SDSS) as well as for fixed stellar template libraries.

for each data set (Indo-US for KCWI and XSL for SDSS) as the fiducial model for that data set, and we report the results of these fiducial fits in Table 2 as $\sigma_{1.5}^{\rm KCWI}$ and $\sigma_{\rm SDSS}^{\rm this\ work}$. For these BIC-preferred libraries, the SDSS velocity dispersions are on average 1.7% ± 2.2% larger than the KCWI values for the same galaxies. Under the assumption of 1.″5 (2.″5) SDSS seeing, the SDSS velocity dispersions are 1.2% ± 2.2% (1.9% ± 2.2%) larger than the KCWI values. For fixed stellar template library, the SDSS velocity dispersions are also larger on average. For Indo-US, the SDSS velocity dispersions are 1.2% ± 1.8% larger than the corresponding KCWI fit. For MILES, which was strongly downweighted by BIC for both KCWI and SDSS, we measure SDSS velocity dispersions that are 5.2% ± 2.2% larger than KCWI. For XSL, SDSS is 2.1% ± 2.1% larger.

As an alternative avenue to evaluate our measured SDSS velocity dispersions and their uncertainties in comparison with the higher-quality KCWI data, we carry out a two-parameter inference to examine any bias as well as residual uncertainties in our SDSS fits when including only the formal statistical uncertainties, as in TDCOSMO-IV. This relies upon our confidence in the KCWI velocity dispersions to determine how much additional uncertainty is appropriate to add to the SDSS errors without assuming the source of those systematics. We include a parameter β to describe any multiplicative bias and a parameter γ to describe underestimated errors in the velocity dispersions extracted from SDSS spectra. The likelihood is then

$$\frac{1}{\sqrt{2\pi}\,\delta\sigma_{\rm T}}\exp\left[-\frac{1}{2}\left(\frac{\sigma_{\rm KCWI,1.5}-\beta\sigma_{\rm SDSS}}{\delta\sigma_{\rm T}}\right)^2\right], \quad (3)$$

where

$$\delta\sigma_{\rm T}^2=\delta\sigma_{\rm KCWI,1.5}^2+(1+\gamma)^2\delta\sigma_{\rm SDSS}^2, \quad (4)$$

or

$$\delta\sigma_{\rm T}^2=\delta\sigma_{\rm KCWI,1.5}^2+\delta\sigma_{\rm SDSS}^2+\gamma_*^2\sigma_{\rm SDSS}^2, \quad (5)$$

Is the total uncertainty of the comparison between our measured velocity dispersion from the SDSS spectra and the one estimated based on the KCWI data within the same aperture with mock seeing. γ in Equation (4) describes a percentage underestimate of the absolute velocity dispersion errors from our SDSS extractions. γ_* in Equation (5) describes the underestimate of the relative SDSS errors by a percentage of the velocity dispersions and is the parameterization as in TDCOSMO-IV (Equation (57)), where the equivalent parameter is called $\sigma_{\sigma^{\rm P},\rm sys}$. β will be very close to the same value for both equations. We optimize the likelihood function using Markov Chain Monte Carlo sampling using the software package[15] EMCEE (J. Goodman & J. Weare 2010; D. Foreman-Mackey et al. 2013). We use a Jeffreys prior of $1/\gamma$ and with $\delta\sigma_{\rm T}^2$ as in Equation (4). In Table 4, we show the inferred values of γ, γ_*, and β by comparing our velocity dispersions measured from KCWI and from SDSS spectra for the fiducial, BIC-preferred libraries (Indo-US for KCWI and XSL for SDSS), as well as for fixed stellar template libraries.

For the fiducial models with the best-BIC template libraries, for the parameters in Equation (4), we find $\gamma = 0.097^{+0.189}_{-0.075}$ and $\beta = 1.002 \pm 0.020$. This again indicates no evidence of bias in the velocity dispersions we measure from SDSS; however, the uncertainties are shown to be underestimated by $9.7\%^{+18.9\%}_{-7.5\%}$ (with respect to the uncertainty) to be added in quadrature to the estimated SDSS uncertainty. Using $\delta\sigma_{\rm T}^2$ as in Equation (5), we find $\gamma_* = 0.039^{+0.027}_{-0.021}$, and β is unchanged. The underestimated error could then be accounted for by adding a relative $3.9\%^{+2.7\%}_{-2.1\%}$ error (with respect to the velocity dispersion) in quadrature. This is consistent with our own estimate of the systematic residual error due to the template library selection shown in Table 3. We find results consistent with this picture when comparing the KCWI and SDSS velocity dispersions when both are fitted with templates from Indo-US or XSL. The MILES library, which was strongly disfavored for both the KCWI and SDSS data sets in our fits by BIC evidence, results in an ∼4% difference between the the data sets ($\beta = 0.957 \pm 0.020$ for Equation (4) and $\beta = 0.959 \pm 0.023$ for Equation (5)). We infer a $5.0\%^{+2.7\%}_{-2.4\%}$ (relative to the velocity dispersions) residual error from the MILES fits. These are consistent within 1σ with our estimated systematic uncertainty from the stellar template library mismatch (see Table 3). Because the differences between our measurements of the KCWI and SDSS data are within the uncertainties on the mean at the sample level, and our SDSS velocity dispersions include both statistical and systematic uncertainties well above these differences, we conclude that there is no measurable bias between the velocity dispersions we measure from the SDSS spectra versus those obtained with the KCWI data, using the same procedure and cleaned stellar libraries. Our analysis shows that a systematic uncertainty of ∼3%–4%, of which the majority is attributable to the stellar template library selection, must be added in quadrature to the errors of our extracted SDSS velocity dispersions. For the ease of interpretation and implementation, we recommend the γ_* model be used to calculate the term to be added in quadrature

[15] https://pypi.org/project/emcee/

to the uncertainties on SDSS velocity dispersions whenever used.

4.2.2. Comparison with Previously Published SDSS Velocity Dispersions

We are now in a position to compare our measured velocity dispersions with the SDSS measurements that have been utilized in TDCOSMO-IV (from SLACS-XII). We also compare with earlier SLACS velocity dispersions extracted from SDSS spectra. SLACS-IX and SLACS-X explore FP relations and other correlations in SLACS galaxies through joint lensing–dynamical inference, using velocity dispersions measured with the ELODIE stellar template library (P. Prugniel & C. Soubiran 2001), which we have not used in any of our analyses. We compare the correlations and other inferred quantities with our KCWI data in Section 5.1. SLACS-XII updated and superseded these velocity dispersions with methodology outlined by A. S. Bolton et al. (2012a) and A. S. Bolton et al. (2012b), using the Indo-US library to cover broader wavelength ranges than were available previously, which represents a change in the most significant contributors to systematic error we find in our methods (see Section 3.1).

Given the superior quality of our data with respect to SDSS, this comparison gives us an opportunity to assess any bias in prior SDSS measurements and by how much the SDSS uncertainties are underestimated, as found by TDCOSMO-IV. We note that these analyses utilized the same spectra we analyzed, which have S/N ~ 9 Å^{-1} and are likely subject to statistical and systematic uncertainties similar to those reported in the bottom row of Table 3, 7.71% statistical and 3.31% systematic, as well as 2.28% covariance over the sample due to the correlated effect of the stellar template libraries. With that in mind, any trend of differences in the fitted velocity dispersions between our measurements and previous velocity dispersions measured from SDSS spectra at 3.31% or less do not indicate a significant measurable bias. We note one object (SDSS J1538+5817) is a strong outlier in our comparisons. We retrieved two observations of this galaxy from SDSS. One yields 180 ± 12 km s^{-1}, which agrees closely with the SLACS-IX and SLACS-XII values. The other yields 253 ± 15 km s^{-1}. The value we measure over the same aperture with KCWI data and mock seeing, 216 ± 2 km s^{-1}, is at the midpoint between these two values. The difference in mean velocity is 22 ± 11 km s^{-1}, suggesting that the two observations are not both pointed at the center of the galaxy, but at least one of the fibers was misaligned. This may explain the difference in velocity dispersion. Therefore we do not consider this object in the comparison here.

The upper panel of Figure 9 shows our measured velocity dispersions for KCWI and SDSS among the single-aperture stellar velocity dispersions for SLACS lenses based on different data sets and apertures. The middle panel compares three different measurements (the KCWI 1.″5 aperture velocity dispersions with mock SDSS seeing in black, our velocity dispersions measured from SDSS spectra in green, and the SLACS-IX velocity dispersion in yellow) against the SLACS-XII velocity dispersions. Averaged over the sample, the KCWI data agree with the SLACS-XII values to $0.5\% \pm 1.3\%$. Our velocity dispersions measured from the SDSS spectra agree with SLACS-XII to an average of $1.4\% \pm 2.3\%$. The SLACS-IX values are higher with respect to SLACS-XII on average by $2.9\% \pm 2.2\%$. The lower panel of the figure shows a comparison between the velocity dispersions from this work compared against SLACS-IX. The KCWI velocity dispersions are smaller than the SLACS-IX values by $4.3\% \pm 1.7\%$, and our measured SDSS velocity dispersions are smaller by $4.5\% \pm 2.7\%$. These differences reflect the systematic uncertainties and covariance we expect for changes in stellar template library given the low S/N of the SDSS spectra, as described in Table 3.

We compare our KCWI velocity dispersions with the published SDSS values with Equations (3)–(5) as in Section 4.2.1. These results are also given in the legends for the middle and lower panels of Figure 9. For the SLACS-XII velocity dispersions, we find $\gamma = 0.062^{+0.162}_{-0.042}$ and $\beta = 0.999 \pm 0.014$. Using Equation (5), we find $\gamma_* = 0.021^{+0.017}_{-0.008}$, and β is unchanged. This again indicates no evidence of bias in the SDSS velocity dispersions measured by SLACS-XII. The uncertainties are shown to be underestimated by a $6.2\%^{+16.2\%}_{-4.2\%}$ (with respect to the uncertainty) or $2.1\%^{+1.7\%}_{-0.8\%}$ error (with respect to the velocity dispersion) to be added in quadrature to the reported uncertainty. This is consistent with our own estimate of the systematic residual errors shown in Table 3. Our estimate of γ_* is somewhat lower than the inference of TDCOSMO-IV, who found $\gamma_* = 0.06 \pm 0.02$, although it is consistent within the errors. We repeat the comparison of KCWI data with SLACS-IX velocity dispersions in the formalism of Equations (3)–(5). We find $\gamma = 0.080^{+0.212}_{-0.062}$, $\gamma_* = 0.023^{+0.010}_{-0.023}$, and $\beta = 0.965 \pm 0.019$, indicating a broad scatter and a $3.5\% \pm 1.9\%$ difference on the mean. We attribute this difference primarily to the update in stellar libraries, but there is no significant bias indicated beyond the level of systematic uncertainty we expect for the SDSS spectra at this S/N.

In summary, we find no measurable bias between the velocity dispersions measured with SDSS spectra when compared with KCWI data for the same galaxies, for previous analyses or for our own. We find the uncertainties of the velocity dispersions measured from the SDSS spectra for our subsample of 13 galaxies to be consistent with the systematic uncertainties attributable to the stellar template library selection that we estimate for the larger SLACS parent sample with similar S/Ns. Furthermore, with the exception of the very highest-S/N spectra, the velocity dispersions of SLACS galaxies measured with SDSS are not suitable for measuring the Hubble constant with precision and accuracy below 2%. Across our sample and in comparison with previous SLACS studies, the velocity dispersions extracted from the SDSS spectra are consistent within the 5% level, which is sufficient for the galaxy formation and evolution purposes for which they were intended. However, we find that the relative uncertainties of the SDSS velocity dispersions are underestimated, and need an additional ∼2%–4% depending on the analysis. Furthermore, the ∼2% covariance that we estimate between our velocity dispersions measured from the SDSS spectra, as a result of the correlated effect of the different stellar template libraries, is significant for H_0. We therefore conclude that the inference in TDCOSMO-IV based on the SLACS SDSS velocity dispersions underestimated the overall uncertainty because while it boosted the individual errors it did not include the covariance. We recommend that future hierarchical cosmological inferences utilize velocity dispersions extracted from higher-S/N spectra with the methods outlined in TDCOSMO-XIX.

Two of our objects were also observed in the XLENS survey (C. Spiniello et al. 2011) and extracted with single-slit

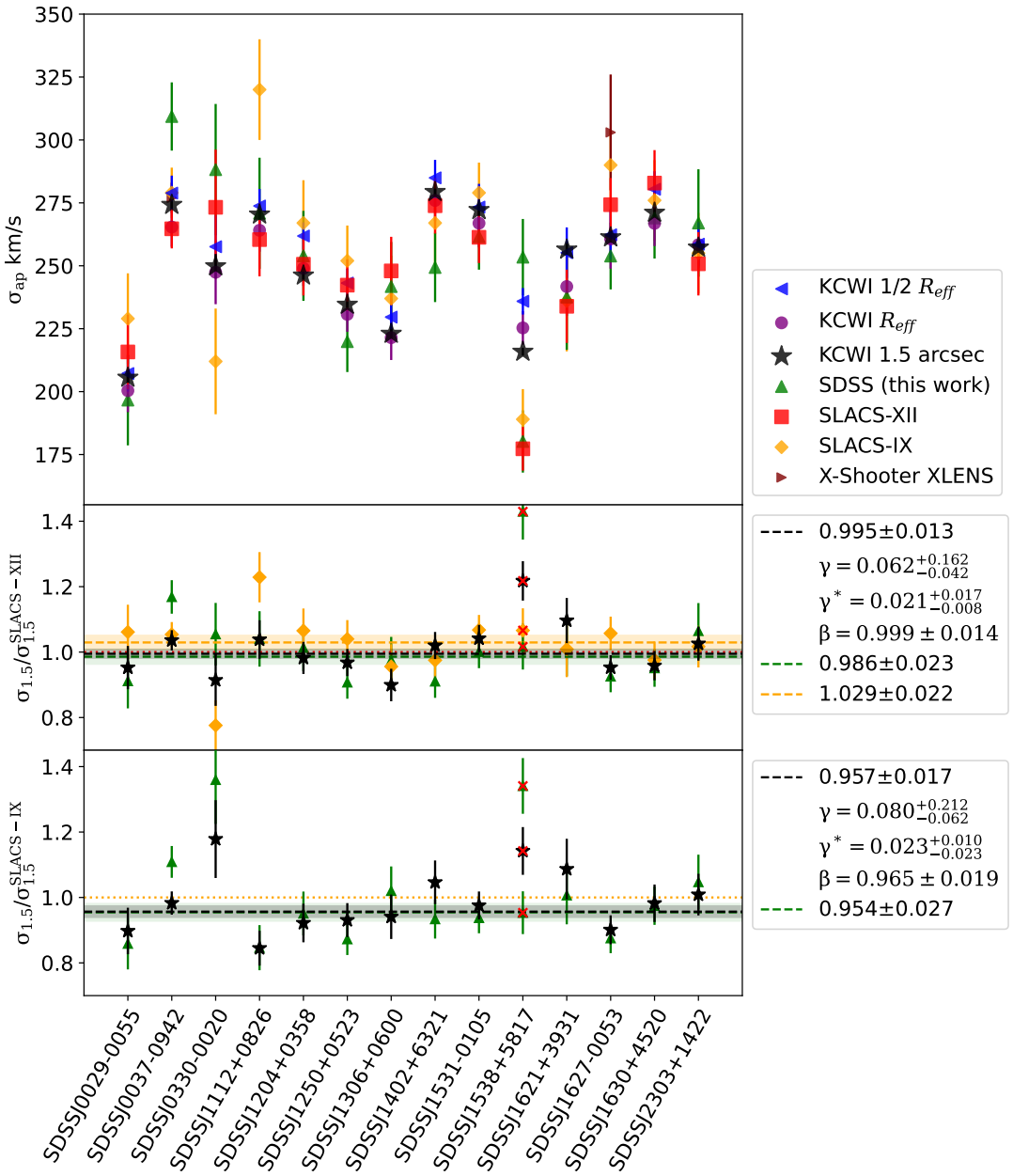

Figure 9. We compare integrated velocity dispersions within various apertures from the KCWI data cubes and those extracted from the SDSS spectra. The blue left-pointing triangle and purple circle markers indicate the velocity dispersions extracted from the kinematic maps by luminosity-weighted integration. These are the values we use, e.g., for the $(V/\sigma, \epsilon)$ and (λ_R, ϵ) calculations and inferences in Section 5.1. We also integrate KCWI kinematics at the data cube level within the SDSS 1.″5 aperture radius (black star) for comparison with kinematics from SDSS-III BOSS fiber spectroscopy: extracted with our methods (green triangle), reported in SLACS-XII (red square), and from SLACS-IX (orange diamond). We also include X-shooter slit-spectroscopy velocity dispersions from XLENS (C. Spiniello et al. 2015) for two objects (maroon right-pointing triangles). In the middle panel of the figure, we plot the ratios of the 1.″5 aperture-integrated KCWI velocity dispersions, our reanalysis of the SDSS spectra, and the SLACS-IX velocity dispersions against the SLACS-XII velocity dispersions. Markers and colors are identical to the upper panel. We inferred parameters γ, γ^*, and β, defined as in Equations (3)–(5) for the comparison between KCWI and SLACS-XII. We remove SDSS J1538+5817 from these inferences, indicated in the plot with a red X, because there may be an issue with the SDSS target centering. The lower plot shows the agreement between our extractions from both KCWI and SDSS when compared with the kinematics from SLACS-IX.

kinematics from X-shooter spectroscopy (C. Spiniello et al. 2015). SDSS J0037-0942 shows excellent agreement between X-shooter and the integrated KCWI velocity dispersions, well within the 1σ uncertainties. SDSS J1627-0053, on the other hand, is $2\sigma \sim 15\%$ larger for the X-shooter velocity dispersions with respect to the KCWI integrated values. Unfortunately, without more overlap between the KCWI SLACS sample and XLENS survey, we are unable to draw significant conclusions from the comparison.

5. Discussion

5.1. Correlations with Other Observables

With updated spatially resolved kinematics and SDSS extractions, we are able to test some inferred quantities against values inferred from SDSS spectra and previous SLACS studies. We take the most recent lens model results for these objects from C. Y. Tan et al. (2024), utilizing their lensing mass power-law slope γ and Einstein radius. Following SLACS-X,

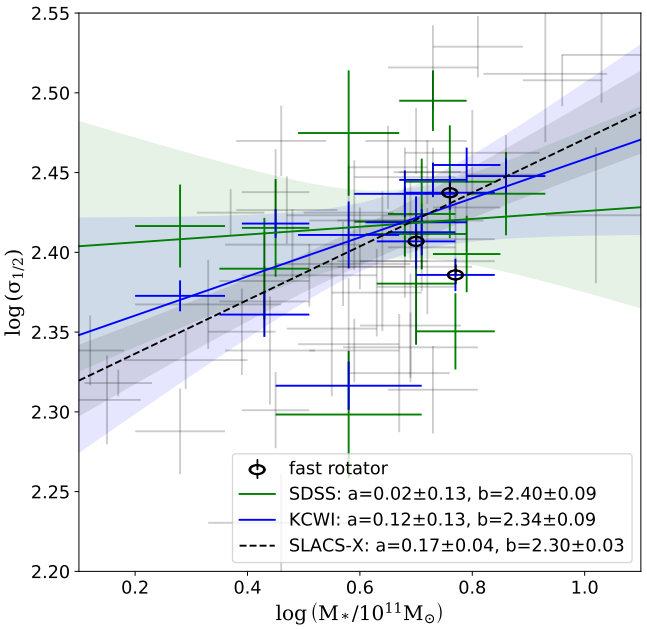

Figure 10. The y-axis shows the $\log_{10}$ of the velocity dispersion within half the effective radius. The x-axis shows the $\log_{10}$ of the stellar mass from stellar population synthesis in units of 10^{11} $M_{\odot}$. KCWI (blue) and SDSS (green) quantities are derived from kinematic extractions in this work for each object in our subsample of 14 SLACS lenses. Gray markers and dotted black lines indicate SLACS-X data and fits. Fast rotators are marked as in Figure 5. Uncertainties on the fits and error bars are 1σ. Fit parameters a and b are the slope and intercept, respectively.

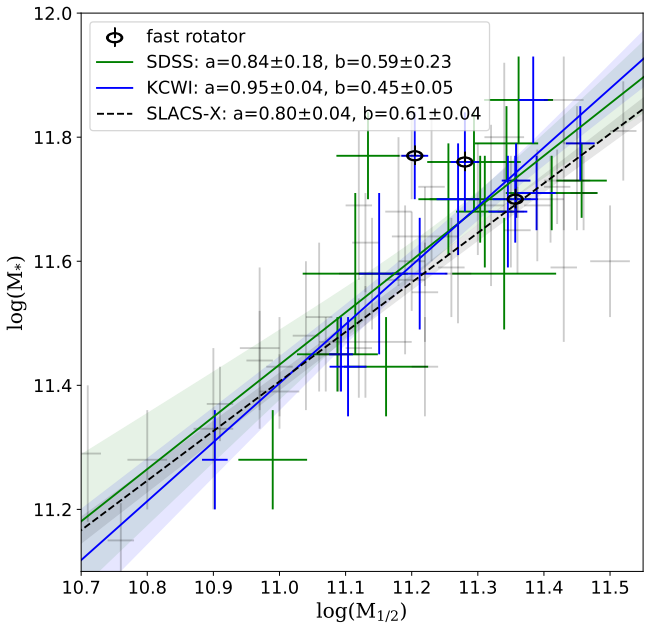

Figure 11. The y-axis shows the $\log_{10}$ of the stellar mass from stellar population synthesis. The x-axis shows the $\log_{10}$ of the virial estimate of the total projected mass within a cylinder of radius half the effective radius. Markers and lines are as defined in Figure 10.

we focus on the centermost region (within half of the effective radius) of the galaxies. We calculate $\sigma_{1/2}$ from our updated SDSS 1.″5 aperture velocity dispersions by the following equation (taking $\sigma_{\rm ap} = \sigma_{\rm eff}(R_{\rm ap}/R_{\rm eff})^{-0.040}$, the power-law fit given in Section 4.2 and shown in Figure 7):

$$\sigma_{1/2} = \sigma_{\rm eff}(1/2)^{-0.040} = \sigma_{1.''5}\left(\frac{1.''5}{R_{\rm eff}}\right)^{0.040},$$

$$(1/2)^{-0.040} = \sigma_{1.''5}\left(\frac{R_{\rm eff}}{3}\right)^{-0.040}.$$

We take all stellar masses from stellar population models assuming a Salpeter initial mass function (IMF) and rest-frame V-band effective radius estimates from SLACS-IX and SLACS-X. $\sigma_{1/2}$ for KCWI targets is integrated from the kinematic map within an aperture radius that is half the effective radius in a flux-weighted average, as described in Section 4.1 and listed in Table 2. In the following Figures 10–14, blue markers indicate KCWI values, and green markers indicate SDSS values. Fainter gray markers indicate the full SLACS sample values from SLACS-IX and SLACS-X. In Section 4.2.1, we found these velocity dispersions to be consistent within 1σ with KCWI observations extracted from the same aperture size. Everything else (effective radius, stellar mass, power-law slope, and Einstein radius) is consistent between the blue and green points. Linear fits are performed for all three samples with NUMPY.POLYFIT and NUMPY.CURVEFIT (C. R. Harris et al. 2020), and we describe them with a (slope) and b (intercept) in the text and figures. Shaded areas denote 1σ confidence levels.

5.1.1. Correlations to Stellar Mass

The stellar mass plane (M_*P; J. B. Hyde & M. Bernardi 2009a) is an extension of the FP where surface brightness is replaced by stellar mass. In general the total mass and central velocity dispersions correlate with stellar mass. SDSS studies (J. B. Hyde & M. Bernardi 2009b; M. Bernardi et al. 2011) revealed a characteristic break in M_*–σ in ETGs at a mass of $M_{\rm crit} = 2 \times 10^{11}$ $M_{\odot}$. M. Cappellari et al. (2013) show this break to describe a transition between fast and slow rotators in ATLAS$^{\rm 3D}$ at masses below and above $M_{\rm crit}$, respectively. Our subsample of 14 SLACS lenses lie above $M_{\rm crit}$. Figure 10 shows the logarithm of the velocity dispersion integrated within half the effective radius $\sigma_{1/2}$ against the log of the stellar mass ($M_*/10^{11}$ $M_{\odot}$) for a Chabrier IMF (compare to Figure 1 in SLACS-X) with 1σ uncertainties. We note that there is evidence for these massive galaxies to have a heavier IMF, closer to the Salpeter IMF (see, e.g., M. W. Auger et al. 2010b; T. Treu et al. 2010; M. Cappellari et al. 2012), which would imply that the true stellar masses may be larger than plotted here by $\sim$0.21 dex. The full sample from SLACS-X is shown in the background as faded gray markers. Blue and green fits indicate fits to our 14 objects using KCWI and SDSS velocity dispersions, respectively. Our data are consistent with the results found for larger samples of SDSS and ATLAS$^{\rm 3D}$ galaxies and are supportive of previously reported M_*P relations.

As in SLACS-X, we define $M_{1/2}$ as the total mass contained within a projected cylinder of radius that is half the effective radius (this is 32% of the total mass for a G. de Vaucouleurs 1948 profile) estimated using the virial relation:

$$M_{1/2} = \frac{C_V R_{\rm eff}\sigma_{1/2}^2}{2G},$$

where $\log_{10} C_V = 0.53 \pm 0.09$ is the virial coefficient. SLACS-X shows $M_{1/2}$ to be tightly linearly correlated with the dynamical mass, and we use $M_{1/2}$ for consistency with their analysis. Figure 11 shows the stellar mass as a

function of $M_{1/2}$ (compare to the centermost plot of Figure 3 in SLACS-X). The tightness of the correlation shows the power of the M_*P and FP. The fits are again consistent with previous studies.

5.1.2. Correlations to Lensing Power-law Slope

Several strong lens studies have found a remarkably good fit to the central total mass density profile of ETGs within a few effective radii with a nearly isothermal power law (e.g., J. D. Cohn et al. 2001; J. A. Muñoz et al. 2001; D. Rusin & C.-P. Ma 2001; D. Rusin et al. 2003; D. Rusin & C. S. Kochanek 2005; A. J. Shajib et al. 2021; A. Etherington et al. 2022; C. Y. Tan et al. 2024). X-ray studies find similar results to scales much larger than the effective radius (e.g., P. A. Thomas 1986; D.-W. Kim & G. Fabbiano 1995; K. Matsushita et al. 1998; P. J. Humphrey & D. A. Buote 2010). Using spatially resolved stellar kinematics from the ATLAS^{3D} and SLUGGS surveys (J. P. Brodie et al. 2014), M. Cappellari et al. (2015) showed the average power-law slope to be very nearly isothermal ($<\gamma> = 2.19 \pm 0.03$) out to 4 $R_{\rm eff}$ in nearby galaxies, with slightly shallower values for galaxies below $\sigma = 100$ km s^{-1} and above $M_{\rm crit} = 2 \times 10^{11}\ M_{\odot}$ (M. Cappellari 2016, Figure 22(c)). Since our subsample of 14 SLACS lenses do not span across these breaks, we expect relations involving the power-law slope γ to agree with previous SLACS findings. L. V. E. Koopmans et al. (2006, 2009) showed through lensing and dynamical analysis that the total mass density profiles of SLACS lenses are well described by a single nearly isothermal power law, and that these do not correlate strongly with other galaxy observables. SLACS-X explored possible correlations between γ and aperture kinematic measurements and found some tentative trends that showed the need for further analysis. The situation has dramatically improved with dynamical analysis with spatially resolved kinematics of large samples of ETGs. K. Zhu et al. (2023) show a steepening of the average slope of the total mass density within the effective radius with increasing velocity dispersion (also within 1 $R_{\rm eff}$) and with age for their MaNGA sample (see their Figure 8). This trend flattens above $\sigma \sim 200$ km s^{-1} where our subsample of SLACS lenses lies, which indicates that we should find negligible trends between power-law slope and kinematic observables if the SLACS subsample is consistent with the MaNGA population.

We discuss possible correlations between lensing power-law slope and kinematics in Figures 12–14 as analogs to the similar discussions in SLACS-X (their Figures 4 and 5). An important distinction is the difference in the definitions of the power-law slope γ between C. Y. Tan et al. (2024) and SLACS-X. The power-law slope γ in SLACS-X (as in ATLAS^{3D}, MaNGA, and earlier SLACS analyses) is defined as the average slope within a certain radius (in SLACS-X, the Einstein radius), while the γ value we take from C. Y. Tan et al. (2024) is defined at the Einstein radius. These plots are comparable to those from SLACS-X only on the surface level, so we do not show SLACS-X data as in Figures 10 and 11. Compared with Figures 10 and 11, the relations we see between KCWI kinematic observables and γ show much more scatter, and correlations are significantly less convincing. C. Y. Tan et al. (2024) rigorously estimate systematic uncertainties in the lens model power-law slopes through a comparison with previous lensing and joint lensing–dynamical studies of the same strong lenses with different codes and assumptions. This could be why the scatter is so high for correlations involving our small subsample of 14 objects. At similar velocity dispersions to

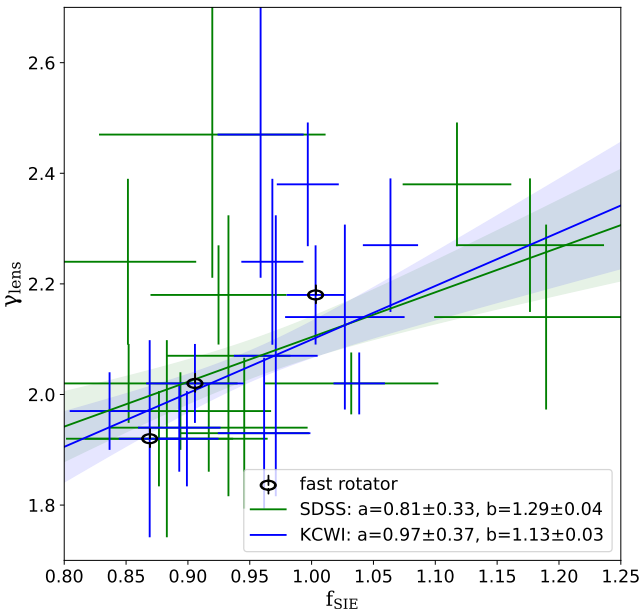

Figure 12. The y-axis shows the slope of the lensing power-law mass density profile at the Einstein radius. The x-axis shows the ratio of the velocity dispersion within half the effective radius to the velocity dispersion calculated from the lens model Einstein radius assuming a singular isothermal ellipse (SIE), $f_{\rm SIE} = \sigma_{1/2}/\sigma_{\rm SIE}$. We do not show SLACS-X data here because the power-law slope is not defined in the same way as in C. Y. Tan et al. (2024). Markers and lines are as defined in Figure 10.

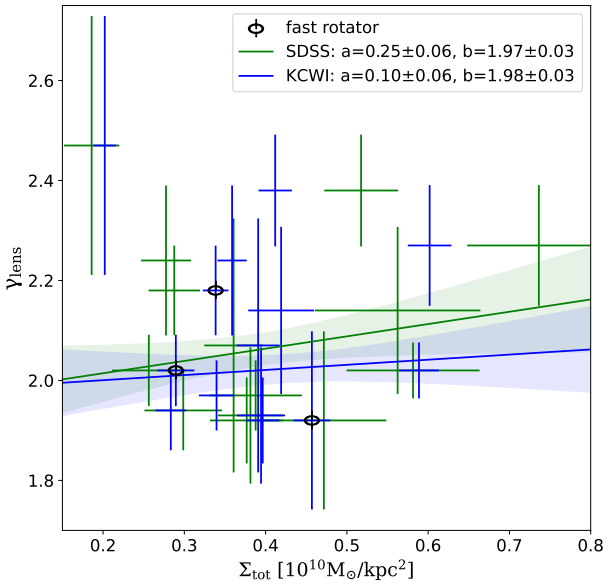

Figure 13. The y-axis shows the slope of the lensing power-law mass density profile at the Einstein radius. The x-axis shows the central surface mass density calculated from the dynamical mass within half the effective radius, $\Sigma_0 \equiv M_{1/2}/R_{\rm eff}^2$. Markers and lines are as defined in Figure 10.

SLACS, MaNGA galaxies have nearly constant slopes $\gamma \sim 2.2$ with a 1σ scatter of 0.2. The lens model power-law slopes γ for our sample are all within 2σ of the MaNGA scatter, as one would expect for a normal population.

In the past, kinematics and lensing data have been compared in the context of less detailed observations. A useful parameter is the deviation of the central velocity dispersion within half the effective radius to the theoretical velocity dispersion for a singular isothermal ellipse (SIE) mass profile model. A value

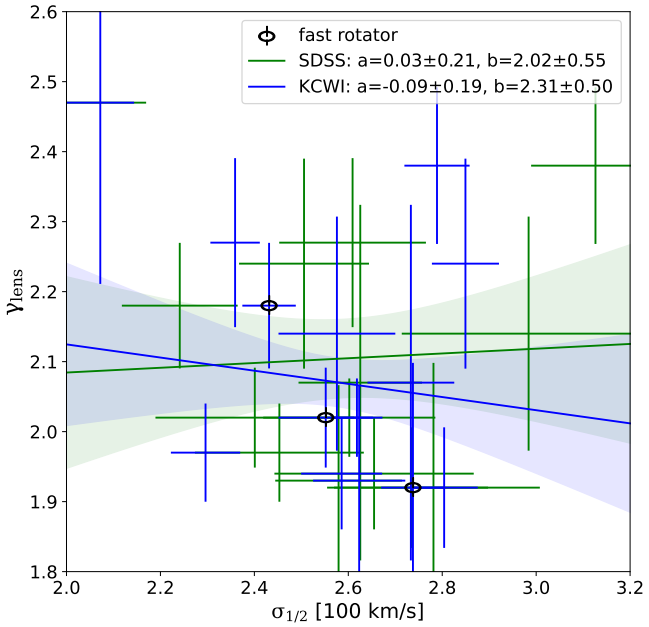

Figure 14. The y-axis shows the slope of the lensing power-law mass density profile at the Einstein radius. The x-axis shows the velocity dispersion within half the effective radius. Markers and lines are as defined in Figure 10.

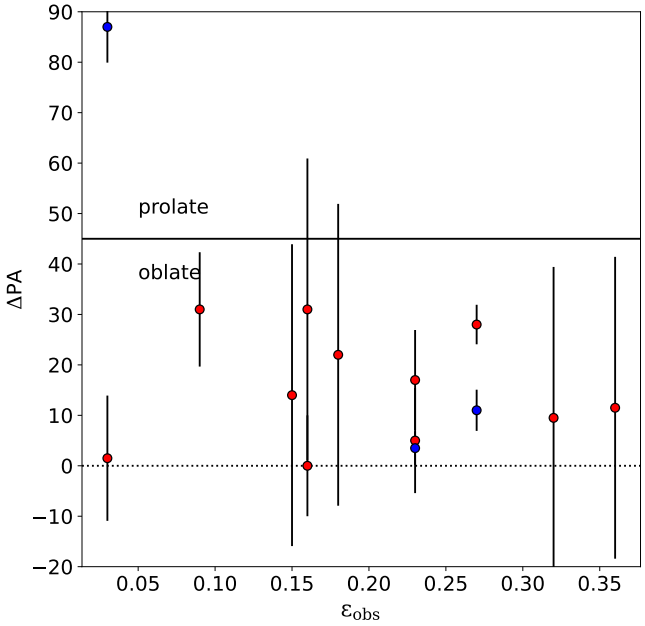

Figure 15. The y-axis shows the misalignment of the photometric and kinematic axes for each object in units of degrees. The x-axis shows the ellipticity of the galaxy measured from the MGE models at the isophote enclosing half the total luminosity. Blue and red markers indicate fast rotators and slow rotators, respectively (see Section 4.1 and Table 2). The kinematic major axis has been measured from mean velocity maps, and the photometric axis is from SLACS-IX. The solid black horizontal line shows the designation between oblate and prolate cases at 45°. All objects are oblate, with the exception of SDSS J1250+0523, which is very round with $\epsilon \sim 0.03$ and likely not truly prolate.

greater than one indicates a mass density profile steeper than isothermal, while a value less than one indicates a flatter slope. T. Treu et al. (2009) found this ratio to be strongly correlated to the mass density power-law slope determined from joint lensing and dynamical models. This relation has been used as a proxy to estimate the power-law slope from kinematics data for which Jeans modeling is unfeasible. SLACS-X found further evidence to support this correlation. We calculate SIE model velocity dispersions from the Einstein radius from lens models from C. Y. Tan et al. (2024):

$$\sigma_{\rm SIE} = \frac{c}{2}\sqrt{\frac{\theta_E}{\pi}\frac{D_{\rm LS}}{D_S}}.$$

We plot the ratio $f_{\rm SIE} = \sigma_{1/2}/\sigma_{\rm SIE}$ against the power-law slope γ from the C. Y. Tan et al. (2024) lens models in Figure 12. We find a milder correlation than the one reported in SLACS-X, who measured a slope of 2.67 ± 0.15. SDSS and KCWI slopes are 0.81 ± 0.33 and 0.97 ± 0.37, respectively. This supports the application of a proxy relation like $f_{\rm SIE}$ as a rough estimate in lieu of the possibility for more complex dynamical analysis. However, as further evidenced in Figures 13 and 14, the scatter in the power-law slope γ is not resolved by these approximations with integrated kinematics.

SLACS-X Figure 5 showed another correlation between γ and the central surface mass density $\Sigma_0 \equiv M_{1/2}/R_{\rm eff}^2$. Our Figure 13 shows on the vertical axis the power-law slope γ, and the horizontal axis is Σ_0 calculated from the virial estimate of projected total central mass $M_{1/2}$ as in Figure 11. The SDSS and KCWI data for our subsample of 14 objects agree on a negligible correlation. We find another negligible correlation when we look at the direct relation between lensing power-law slope γ and the integrated velocity dispersion within half the effective radius $\sigma_{1/2}$ in Figure 14, in agreement with SLACS-X. When compared with the MaNGA DynPop sample in K. Zhu et al. (2023), we see that our SLACS subsample lies in the region where γ is nearly constant, indicating consistent populations in the observed mass range.

5.2. Axisymmetric versus Triaxial

An important factor for the dynamical interpretation of the kinematics is the alignment of photometric and kinematic axes. The kinematic major axis has been measured from mean velocity maps using the `PaFit` package[16] (D. Krajnović et al. 2006), and the photometric position angle is from HST photometry as reported in A. S. Bolton et al. (2008a). In Figure 15, we show the angle between misalignment of these axes ΔPA for each object as a function of observed ellipticity. Observed ellipticity is measured from the MGE models at the isophote enclosing half the total luminosity, using the procedure `mge_half_light_isophote` from the JAM software package.[17] Blue markers indicate objects we identify as fast rotators (see Section 4.1 and Table 2), which have significantly better constrained kinematic axes than the objects we identify as slow rotators (shown here in red markers). The dominant uncertainty in ΔPA comes from the kinematic major axis, which is poorly defined for slow rotators that do not show any regular rotation. Photometric uncertainty is not published in the SLACS papers, so it cannot be added. However, based on experience and data quality it is much smaller than that of the kinematic axis and therefore negligible for this comparison. Misalignments $0 < |\Delta{\rm PA}| < 45$ are considered most likely axisymmetric and oblate, and $45 < |\Delta{\rm PA}| < 90$ are most likely triaxial or prolate. The solid black horizontal line shows this separation. We note one fast rotator (SDSS J1250 +0523) that appears to show prolate rotation due to its nearly 90° measured misalignment. This object is very round with an

[16] https://pypi.org/project/pafit/
[17] https://pypi.org/project/jampy/

observed ellipticity $\epsilon_{\rm obs} \sim 0.03$, so the photometric axis may be highly uncertain.

5.3. Time-delay Cosmography

The kinematic maps and analysis in this work illustrate that the KCWI data are of sufficient quality to achieve strong constraints on the mass profiles and anisotropy of lensing ETGs. Correlations also highlight the need for this quality of data and more detailed dynamical analysis, which will be presented in the upcoming companion paper. The 1% off-diagonal term of the covariance matrix at the sample level indicates that 2% precision on H_0 is achievable given an expanded sample of non-time-delay lenses of the same level of quality. Improved data sets with an expanded SLACS sample (e.g., with the new KCRM red arm of KCWI) will improve constraints from the non-time-delay data beyond this 2% level. Complementary to parallel ongoing kinematic measurements with KCWI of time-delay lenses (e.g., TDCOSMO-XII), we project that the combined sample of our measurements with time-delay lenses will help to achieve a precision for H_0 that is independent of the best current determinations of H_0 based on the local distance ladder (W. L. Freedman 2021; A. G. Riess et al. 2022) and comparably precise (1.9%, using the same methodology as S. Birrer & T. Treu 2021, and updated based on ongoing and scheduled observations). It will also provide a key verification of the TDCOSMO 2% precision measurement (M. Millon et al. 2020b) achieved under mass density profile assumptions.

6. Conclusions

We present kinematic data and analysis for 14 SLACS strong gravitational lens deflector galaxies, from which we determine the following main conclusions.

1. Most (11) of our 14 SLACS lenses are consistent in terms of (V/σ, ϵ) and ($\lambda_{\rm R}$, ϵ) with the round "slow" nonregular rotators of the local Universe (as in ATLAS$^{\rm 3D}$), with the exception of three that have significant rotational support and are close to the boundary between "slow" and "fast" regular rotators.
2. We quantify the systematic error at the spatial bin level for each object and find a 1%–1.4% systematic error, dominated by the template library choice. At the sample level, we find a positive covariance of <1% that indicates that with current kinematics the SLACS sample is sufficient to achieve hierarchical inference of H_0 to 2% precision.
3. Systematics between velocity dispersions extracted from SDSS spectra of the SLACS galaxies are at the level of 2%–4% with positive sample covariance of ∼2% depending on the S/N of the spectra, primarily due to the stellar template library selection. Relative uncertainties of previously published SDSS velocity dispersions for these 14 galaxies are underestimated by ∼2%–3%. We therefore conclude that they are sufficiently accurate for galaxy studies, but that their systematics and covariance are significant for accurate time-delay cosmography. Case in point, the TDCOSMO + SLACS measurement of $H_0 = 67.4^{+4.1}_{-3.2}$ km s^{-1} Mpc^{-1} reported by TDCOSMO-IV based on SDSS velocity dispersions neglects the covariance among the SDSS velocity dispersion measurements and thus overestimates the constraining power of the SDSS sample, resulting in underestimated uncertainties and a potential bias in the inferred value of H_0. We recommend that future hierarchical cosmological inferences utilize velocity dispersions extracted from higher-S/N spectra with the methods outlined in TDCOSMO-XIX.
4. ETG scaling relations are overall consistent with previous SLACS studies. In particular:
   1. stellar mass correlates positively with velocity dispersion and central projected total mass, agreeing within the $1\,\sigma$ uncertainty with the correlations published in SLACS-X;
   2. the lensing power-law slope correlates mildly with $f_{\rm SIE}$ (deviation from SIE velocity dispersion) with a slope of 0.97 ± 0.37; and
   3. the lensing power-law slope shows no correlation with the surface mass density or central velocity dispersion.

These kinematic data are prepared for dynamical fitting with JAM (M. Cappellari 2008, 2020). The result of this approach will produce constraints on the mass profiles and anisotropy of ETGs, which will in turn help to constrain the Hubble constant through time-delay cosmography of distant lensed quasars.

Acknowledgments

We acknowledge support by the National Science Foundation in the form of a graduate fellowship to S.K., and grants NSF-AST-2407277, NSF-AST-1906976, NSF-AST-1836016, NSF-AST-1909297, and NSF-AST-2407277. Note that findings and conclusions do not necessarily represent views of the NSF. We also acknowledge support by the Gordon and Betty Moore Foundation through a grant to T.T.

We thank A.S. Bolton and M.Bernardi for useful discussions regarding SDSS velocity dispersions.

Some of the data presented herein were obtained at Keck Observatory, which is a private 501(c)3 nonprofit organization operated as a scientific partnership among the California Institute of Technology, the University of California, and the National Aeronautics and Space Administration. The Observatory was made possible by the generous financial support of the W. M. Keck Foundation. The authors wish to recognize and acknowledge the very significant cultural role and reverence that the summit of Maunakea has always had within the Native Hawaiian community. We are most fortunate to have the opportunity to conduct observations from this mountain.

This research is based in part on observations made with the NASA/ESA Hubble Space Telescope obtained from the Space Telescope Science Institute, which is operated by the Association of Universities for Research in Astronomy, Inc., under NASA contract NAS 5–26555. These observations are associated with program(s) 10174 (PI: L. Koopmans), 10886 (PI: A. Bolton), 10494 (PI: L. Koopmans), and 10587 (PI: A. Bolton).

The HST data presented in this article were obtained from the Mikulski Archive for Space Telescopes (MAST) at the Space Telescope Science Institute. The specific observations analyzed can be accessed via DOI:10.17909/nrbe-b166.

ORCID iDs

Shawn Knabel https://orcid.org/0000-0001-5110-6241
Tommaso Treu https://orcid.org/0000-0002-8460-0390
Michele Cappellari https://orcid.org/0000-0002-1283-8420
Anowar J. Shajib https://orcid.org/0000-0002-5558-888X
Simon Birrer https://orcid.org/0000-0003-3195-5507
Vardha N. Bennert https://orcid.org/0000-0003-2064-0518

References

Abdalla, E., Abellán, G. F., Aboubrahim, A., et al. 2022, JHEAp, 34, 49
Abdurro'uf, Accetta, K., Aerts, C., et al. 2022, ApJS, 259, 35
Auger, M. W., Treu, T., Bolton, A. S., et al. 2009, ApJ, 705, 1099
Auger, M. W., Treu, T., Bolton, A. S., et al. 2010a, ApJ, 724, 511
Auger, M. W., Treu, T., Gavazzi, R., et al. 2010b, ApJL, 721, L163
Avila, R., Koekemoer, A., Mack, J., & Fruchter, A. 2015, Optimizing pixfrac in Astrodrizzle: An example from the Hubble Frontier Fields, Instrument Science Report WFC3 2015-04, STScI
Bacon, R., Accardo, M., Adjali, L., et al. 2010, Proc. SPIE, 7735, 773508
Bacon, R., Adam, G., Baranne, A., et al. 1995, A&AS, 113, 347
Bacon, R., Copin, Y., Monnet, G., et al. 2001, MNRAS, 326, 23
Barnabè, M., Czoske, O., Koopmans, L. V. E., Treu, T., & Bolton, A. S. 2011, MNRAS, 415, 2215
Barnabè, M., Czoske, O., Koopmans, L. V. E., et al. 2009, MNRAS, 399, 21
Barth, A. J., Ho, L. C., & Sargent, W. L. W. 2002, AJ, 124, 2607
Bennert, V. N., Treu, T., Auger, M. W., et al. 2015, ApJ, 809, 20
Bernardi, M., Roche, N., Shankar, F., & Sheth, R. K. 2011, MNRAS, 412, L6
Bertola, F., & Capaccioli, M. 1975, ApJ, 200, 439
Bevacqua, D., Cappellari, M., & Pellegrini, S. 2022, MNRAS, 511, 139
Bezanson, R., van Dokkum, P. G., Tal, T., et al. 2009, ApJ, 697, 1290
Binney, J. 1978, MNRAS, 183, 501
Binney, J. 2005, MNRAS, 363, 937
Binney, J., & Mamon, G. A. 1982, MNRAS, 200, 361
Birrer, S., Millon, M., Sluse, D., et al. 2024, SSRv, 220, 48
Birrer, S., Shajib, A. J., Galan, A., et al. 2020, A&A, 643, A165
Birrer, S., & Treu, T. 2021, A&A, 649, A61
Birrer, S., Treu, T., Rusu, C. E., et al. 2019, MNRAS, 484, 4726
Bolton, A. S., Brownstein, J. R., Kochanek, C. S., et al. 2012a, ApJ, 757, 82
Bolton, A. S., Burles, S., Koopmans, L. V. E., Treu, T., & Moustakas, L. A. 2006, ApJ, 638, 703
Bolton, A. S., Burles, S., Koopmans, L. V. E., et al. 2008a, ApJ, 682, 964
Bolton, A. S., Burles, S., Treu, T., Koopmans, L. V. E., & Moustakas, L. A. 2007, ApJL, 665, L105
Bolton, A. S., Schlegel, D. J., Aubourg, É., et al. 2012b, AJ, 144, 144
Bolton, A. S., Treu, T., Koopmans, L. V. E., et al. 2008b, ApJ, 684, 248
Bonvin, V., Courbin, F., Suyu, S. H., et al. 2017, MNRAS, 465, 4914
Brodie, J. P., Romanowsky, A. J., Strader, J., et al. 2014, ApJ, 796, 52
Bryant, J. J., Owers, M. S., Robotham, A. S. G., et al. 2015, MNRAS, 447, 2857
Bundy, K., Bershady, M. A., Law, D. R., et al. 2015, ApJ, 798, 7
Burkert, A., & Naab, T. 2004, in Carnegie Observatories Centennial Symp., Coevolution of Black Holes and Galaxies, ed. L. C. Ho (Cambridge: Cambridge Univ. Press), 421
Cappellari, M. 2002, MNRAS, 333, 400
Cappellari, M. 2008, MNRAS, 390, 71
Cappellari, M. 2016, ARA&A, 54, 597
Cappellari, M. 2017, MNRAS, 466, 798
Cappellari, M. 2020, MNRAS, 494, 4819
Cappellari, M. 2023, MNRAS, 526, 3273
Cappellari, M., Bacon, R., Bureau, M., et al. 2006, MNRAS, 366, 1126
Cappellari, M., & Copin, Y. 2003, MNRAS, 342, 345
Cappellari, M., & Emsellem, E. 2004, PASP, 116, 138
Cappellari, M., Emsellem, E., Bacon, R., et al. 2007, MNRAS, 379, 418
Cappellari, M., Emsellem, E., Krajnović, D., et al. 2011, MNRAS, 416, 1680
Cappellari, M., McDermid, R. M., Alatalo, K., et al. 2012, Natur, 484, 485
Cappellari, M., McDermid, R. M., Alatalo, K., et al. 2013, MNRAS, 432, 1862
Cappellari, M., Romanowsky, A. J., Brodie, J. P., et al. 2015, ApJL, 804, L21
Chen, Q., Meyer, M., Popping, A., & Staveley-Smith, L. 2021, MNRAS, 502, 2308
Chen, Y.-M., Shi, Y., Wild, V., et al. 2019, MNRAS, 489, 5709
Cheung, E., Faber, S. M., Koo, D. C., et al. 2012, ApJ, 760, 131
Cohn, J. D., Kochanek, C. S., McLeod, B. A., & Keeton, C. R. 2001, ApJ, 554, 1216
Collett, T. E., Oldham, L. J., Smith, R. J., et al. 2018, Sci, 360, 1342
Courbin, F., Eigenbrod, A., Vuissoz, C., Meylan, G., & Magain, P. 2005, in IAU Symp. 225, Gravitational Lensing Impact on Cosmology, ed. Y. Mellier & G. Meylan (Cambridge: Cambridge University Press), 297
Czoske, O., Barnabè, M., Koopmans, L. V. E., Treu, T., & Bolton, A. S. 2008, MNRAS, 384, 987
Czoske, O., Barnabè, M., Koopmans, L. V. E., Treu, T., & Bolton, A. S. 2012, MNRAS, 419, 656
D'Ago, G., Spiniello, C., Coccato, L., et al. 2023, A&A, 672, A17
Davidson, R., & Flachaire, E. 2008, Journal of Econometrics, 146, 162
De Lucia, G., Springel, V., White, S. D. M., Croton, D., & Kauffmann, G. 2006, MNRAS, 366, 499
de Vaucouleurs, G. 1948, AnAp, 11, 247
de Zeeuw, P. T., Bureau, M., Emsellem, E., et al. 2002, MNRAS, 329, 513
Djorgovski, S., & Davis, M. 1987, ApJ, 313, 59
Dressler, A. 1979, ApJ, 231, 659
Dressler, A. 1984, ApJ, 286, 97
Dressler, A., Faber, S. M., Burstein, D., et al. 1987, ApJL, 313, L37
Emsellem, E., Cappellari, M., Krajnović, D., et al. 2007, MNRAS, 379, 401
Emsellem, E., Cappellari, M., Krajnović, D., et al. 2011, MNRAS, 414, 888
Emsellem, E., Cappellari, M., Peletier, R. F., et al. 2004, MNRAS, 352, 721
Emsellem, E., Monnet, G., Bacon, R., & Nieto, J. L. 1994, A&A, 285, 739
Etherington, A., Nightingale, J. W., Massey, R., et al. 2022, MNRAS, 517, 3275
Faber, S. M., & Jackson, R. E. 1976, ApJ, 204, 668
Faber, S. M., Tremaine, S., Ajhar, E. A., et al. 1997, AJ, 114, 1771
Falco, E. E., Gorenstein, M. V., & Shapiro, I. I. 1985, ApJL, 289, L1
Falcón-Barroso, J., Lyubenova, M., & van de Ven, G. 2015, in IAU Symp. 311, Galaxy Masses as Constraints of Formation Models, ed. M. Cappellari & S. Courteau (Cambridge: Cambridge Univ. Press), 78
Falcón-Barroso, J., Sánchez-Blázquez, P., Vazdekis, A., et al. 2011, A&A, 532, A95
Falcón-Barroso, J., van de Ven, G., Lyubenova, M., et al. 2019, A&A, 632, A59
Fang, J. J., Faber, S. M., Koo, D. C., & Dekel, A. 2013, ApJ, 776, 63
Foreman-Mackey, D., Hogg, D. W., Lang, D., & Goodman, J. 2013, PASP, 125, 306
Freedman, W. L. 2021, ApJ, 919, 16
Fruchter, A. S., & Hook, R. N. 2002, PASP, 114, 144
Gilman, D., Birrer, S., & Treu, T. 2020, A&A, 642, A194
Goodman, J., & Weare, J. 2010, CAMCS, 5, 65
Graham, A. W. 2013, in Planets, Stars and Stellar Systems Vol. 6, ed. T. D. Oswalt & W. C. Keel (Dordrecht: Springer), 91
Graham, M. T., Cappellari, M., Li, H., et al. 2018, MNRAS, 477, 4711
Greene, J. E., Leauthaud, A., Emsellem, E., et al. 2017, ApJL, 851, L33
Harris, C. R., Millman, K. J., van der Walt, S. J., et al. 2020, Natur, 585, 357
Hopkins, P. F., Croton, D., Bundy, K., et al. 2010, ApJ, 724, 915
Hubble, E. P. 1926, ApJ, 64, 321
Humphrey, P. J., & Buote, D. A. 2010, MNRAS, 403, 2143
Hyde, J. B., & Bernardi, M. 2009a, MNRAS, 396, 1171
Hyde, J. B., & Bernardi, M. 2009b, MNRAS, 394, 1978
Illingworth, G. 1977, ApJL, 218, L43
Jorgensen, I., Franx, M., & Kjaergaard, P. 1996, MNRAS, 280, 167
Kelson, D. D., Illingworth, G. D., van Dokkum, P. G., & Franx, M. 2000, ApJ, 531, 159
Kim, D.-W., & Fabbiano, G. 1995, ApJ, 441, 182
Knabel, S., Mozumdar, P., Shajib, A. J., et al. 2025, arXiv:2502.16034
Knabel, S., Steele, R. L., Holwerda, B. W., et al. 2020, AJ, 160, 223
Koopmans, L. V. E., Bolton, A., Treu, T., et al. 2009, ApJL, 703, L51
Koopmans, L. V. E., Treu, T., Bolton, A. S., Burles, S., & Moustakas, L. A. 2006, ApJ, 649, 599
Kormendy, J. 1977, ApJ, 217, 406
Kormendy, J., & Bender, R. 1996, ApJL, 464, L119
Kormendy, J., & Bender, R. 2009, ApJL, 691, L142
Kormendy, J., & Bender, R. 2012, ApJS, 198, 2
Kormendy, J., & Freeman, K. C. 2016, ApJ, 817, 84
Kormendy, J., & Illingworth, G. 1982, ApJ, 256, 460
Krajnovic, D. 2011, PhyW, 24, 26
Krajnović, D., Cappellari, M., de Zeeuw, P. T., & Copin, Y. 2006, MNRAS, 366, 787
Matsushita, K., Makishima, K., Ikebe, Y., et al. 1998, ApJL, 499, L13
McLean, I. S., Steidel, C. C., Epps, H., et al. 2010, Proc. SPIE, 7735, 77351E
McLean, I. S., Steidel, C. C., Epps, H. W., et al. 2012, Proc. SPIE, 8446, 84460J
Mehlert, D., Thomas, D., Saglia, R. P., Bender, R., & Wegner, G. 2003, A&A, 407, 423

Mehrgan, K., Thomas, J., Saglia, R., Parikh, T., & Bender, R. 2023, ApJ, 948, 79
Millon, M., Courbin, F., Bonvin, V., et al. 2020a, A&A, 640, A105
Millon, M., Galan, A., Courbin, F., et al. 2020b, A&A, 639, A101
Morrissey, P., Matuszewski, M., Martin, C., et al. 2012, Proc. SPIE, 8446, 844613
Morrissey, P., Matuszewski, M., Martin, D. C., et al. 2018, ApJ, 864, 93
Muñoz, J. A., Kochanek, C. S., & Keeton, C. R. 2001, ApJ, 558, 657
Murphy, E. J., Condon, J. J., Schinnerer, E., et al. 2011, ApJ, 737, 67
Naab, T., Johansson, P. H., & Ostriker, J. P. 2009, ApJL, 699, L178
Prugniel, P., & Soubiran, C. 2001, A&A, 369, 1048
Querejeta, M., Meidt, S. E., Schinnerer, E., et al. 2015, ApJS, 219, 5
Refsdal, S. 1964, MNRAS, 128, 307
Renzini, A. 2006, ARA&A, 44, 141
Richstone, D. O., & Tremaine, S. 1988, ApJ, 327, 82
Riess, A. G., Yuan, W., Macri, L. M., et al. 2022, ApJL, 934, L7
Rix, H.-W., de Zeeuw, P. T., Cretton, N., van der Marel, R. P., & Carollo, C. M. 1997, ApJ, 488, 702
Rusin, D., & Kochanek, C. S. 2005, ApJ, 623, 666
Rusin, D., Kochanek, C. S., & Keeton, C. R. 2003, ApJ, 595, 29
Rusin, D., & Ma, C.-P. 2001, ApJL, 549, L33
Rusu, C. E., Wong, K. C., Bonvin, V., et al. 2020, MNRAS, 498, 1440
Sánchez-Blázquez, P., Peletier, R. F., Jiménez-Vicente, J., et al. 2006, MNRAS, 371, 703
Sandage, A. 1975, PASP, 87, 853
Sandage, A. 2005, ARA&A, 43, 581
Schmidt, T., Treu, T., Birrer, S., et al. 2023, MNRAS, 518, 1260
Schneider, P., & Sluse, D. 2013, A&A, 559, A37
Schneider, P., & Sluse, D. 2014, A&A, 564, A103
Schwarzschild, M. 1979, ApJ, 232, 236
Shajib, A. J., Mozumdar, P., Chen, G. C. F., et al. 2023, A&A, 673, A9
Shajib, A. J., Treu, T., & Agnello, A. 2018, MNRAS, 473, 210
Shajib, A. J., Treu, T., Birrer, S., & Sonnenfeld, A. 2021, MNRAS, 503, 2380
Shajib, A. J., Wong, K. C., Birrer, S., et al. 2022, A&A, 667, A123
Shu, Y., Bolton, A. S., Brownstein, J. R., et al. 2015, ApJ, 803, 71
Spiniello, C., Koopmans, L. V. E., Trager, S. C., Czoske, O., & Treu, T. 2011, MNRAS, 417, 3000
Spiniello, C., Koopmans, L. V. E., Trager, S. C., et al. 2015, MNRAS, 452, 2434
Spiniello, C., Tortora, C., D'Ago, G., et al. 2021a, A&A, 646, A2 8
Spiniello, C., Tortora, C., D'Ago, G., et al. 2021b, A&A, 654, A136
Suyu, S. H., Bonvin, V., Courbin, F., et al. 2017, MNRAS, 468, 2590
Tan, C. Y., Shajib, A. J., Birrer, S., et al. 2024, MNRAS, 530, 1474
Thomas, P. A. 1986, MNRAS, 220, 949
Treu, T., Agnello, A., Baumer, M. A., et al. 2018, MNRAS, 481, 1041
Treu, T., Auger, M. W., Koopmans, L. V. E., et al. 2010, ApJ, 709, 1195
Treu, T., Gavazzi, R., Gorecki, A., et al. 2009, ApJ, 690, 67 0
Treu, T., Koopmans, L. V., Bolton, A. S., Burles, S., & Moustakas, L. A. 2006, ApJ, 640, 662
Treu, T., & Koopmans, L. V. E. 2002, MNRAS, 337, L6
Treu, T., & Marshall, P. J. 2016, A&ARv, 24, 11
Treu, T., Stiavelli, M., Møller, P., Casertano, S., & Bertin, G. 2001, MNRAS, 326, 221
Treu, T., Suyu, S. H., & Marshall, P. J. 2022, A&ARv, 30, 8
Valdes, F., Gupta, R., Rose, J. A., Singh, H. P., & Bell, D. J. 2004, ApJS, 152, 251
van de Sande, J., Bland-Hawthorn, J., Brough, S., et al. 2017, MNRAS, 472, 1272
Van de Vyvere, L., Gomer, M. R., Sluse, D., et al. 2022a, A&A, 659, A127
Van de Vyvere, L., Sluse, D., Gomer, M. R., & Mukherjee, S. 2022b, A&A, 663, A179
van der Marel, R. P., Cretton, N., de Zeeuw, P. T., & Rix, H.-W. 1998, ApJ, 493, 613
Verro, K., Trager, S. C., Peletier, R. F., et al. 2022, A&A, 660, A34
Westfall, K. B., Cappellari, M., Bershady, M. A., et al. 2019, AJ, 158, 231
Wong, K. C., Suyu, S. H., Chen, G. C. F., et al. 2020, MNRAS, 498, 1420
Yıldırım, A., Suyu, S. H., Chen, G. C. F., & Komatsu, E. 2023, A&A, 675, A21
Yıldırım, A., Suyu, S. H., & Halkola, A. 2020, MNRAS, 493, 4783
Zhu, K., Lu, S., Cappellari, M., et al. 2023, MNRAS, 522, 6326